

# Comparison of the Shakhov and ellipsoidal models for the Boltzmann equation and DSMC for *ab initio*-based particle interactions

Victor E. Ambruş<sup>a,b</sup>, Felix Sharipov<sup>c</sup>, Victor Sofonea<sup>d</sup>

<sup>a</sup>*Department of Physics, West University of Timișoara, Bd. Vasile Pârvan 4, Timișoara 300223, Romania*

<sup>b</sup>*Department of Mathematics and Statistics, Old Dominion University, Norfolk, VA 23529, USA*

<sup>c</sup>*Departamento de Física, Universidade Federal do Paraná, Curitiba, 81531-980 Brazil*

<sup>d</sup>*Center for Fundamental and Advanced Technical Research, Romanian Academy, Bd. Mihai Viteazu 24, Timișoara 300223, Romania*

---

## Abstract

In this paper, we consider the capabilities of the Boltzmann equation with the Shakhov or ellipsoidal models for the collision term to capture the characteristics of rarefied gas flows. The benchmark is performed by comparing the results obtained using these kinetic model equations with direct simulation Monte Carlo (DSMC) results for particles interacting via *ab initio* potentials. The analysis is restricted to channel flows between parallel plates and we consider three flow problems, namely: the heat transfer between stationary plates, the Couette flow and the heat transfer under shear. The simulations are performed in the non-linear regime for the  $^3\text{He}$ ,  $^4\text{He}$ , and Ne gases. The reference temperature ranges between 1 K and 3000 K for  $^3\text{He}$  and  $^4\text{He}$  and between 20 K and 5000 K for Ne. While good agreement is seen up to the transition regime for the direct phenomena (shear stress, heat flux driven by temperature gradient), the relative errors in the cross phenomena (heat flux perpendicular to the temperature gradient) exceed 10% even in the slip-flow regime. The kinetic model equations are solved using the finite difference lattice Boltzmann algorithm based on half-

---

*Email addresses:* [victor.ambrus@e-uvt.ro](mailto:victor.ambrus@e-uvt.ro) (Victor E. Ambruş),  
[sharipov@fisica.ufpr.br](mailto:sharipov@fisica.ufpr.br) (Felix Sharipov), [sofonea@gmail.com](mailto:sofonea@gmail.com),  
[sofonea@acad-tim.tm.edu.ro](mailto:sofonea@acad-tim.tm.edu.ro) (Victor Sofonea)

range Gauss-Hermite quadratures with the third order upwind method used for the implementation of the advection.

*Keywords:* Ab initio, DSMC, Ellipsoidal model, Shakhov model, Half-range Gauss-Hermite quadrature

---

## 1. Introduction

Finding accurate solutions of the kinetic equations governing rarefied gas flows is a challenging task because of their complexity [1, 2]. In the case of channel flows, it has been shown under quite general assumptions that the velocity field in the vicinity of solid boundaries is non-analytic, its normal derivative presenting a logarithmic singularity with respect to the distance to the wall [3]. Understanding the main properties of such flows is crucial when devising micro/nano-electro-mechanical systems (MEMS/NEMS) [4].

Since the kinetic equation is difficult to solve analytically (in closed form), numerical methods remain the primary tool available for its investigation. It has been established in the research community that the direct simulation Monte Carlo (DSMC) method [5] can provide solutions to realistic systems in a wide range of flow regimes. The main ingredient controlling the relevance of the DSMC formulation lies in specifying the interparticle interactions. Recently, *ab initio* potentials have been implemented into the DSMC method [6, 7, 8, 9]. A quantum consideration of interatomic collisions [10, 11] allowed to extend an application of *ab initio* potentials to low temperatures. To reduce the computational effort, lookup tables for the deflection angle of binary collisions of helium-3 ( $^3\text{He}$ ), helium-4 ( $^4\text{He}$ ), and neon (Ne) atoms have been calculated and reported in the Supplementary material to Ref. [11]. The lookup tables can be used for any flow of these gases over a wide range of temperature. Due to the stochastic nature of the DSMC method, its results often exhibit steady-state fluctuations, which are especially significant in the slip-flow regime and at small Mach numbers. Filtering out these fluctuations is a computationally demanding part of the algorithm, making this method computationally convenient only in

the transition and free molecular regimes.

Another approach for the description of rarefied gas flows starts from the Boltzmann equation, where the collision integral takes into account the details of the interparticle interactions. While recent years have seen significant progress in the development of numerical methods for evaluating the Boltzmann collision integral [12, 13, 14, 15], this operation still remains the most expensive part of the solver, making the application of such methods for complex systems computationally prohibitive.

As argued in the early '50s, the features of the collision integral can be preserved, at least for small Knudsen numbers and mildly non-linear systems, by replacing the collision term through a relaxation time approach. The BGK model, introduced by Bhatnagar, Gross and Krook [16], employed a single relaxation time  $\tau$  to control the departure of the Boltzmann distribution function  $f$  from local thermal equilibrium. This parameter could be used to match realistic flows by ensuring the correct recovery of the dynamic viscosity  $\mu$  in the hydrodynamic regime, however it could not allow the heat conductivity  $\kappa$  to be controlled independently. This difficulty was later alleviated through two extensions, known as the ellipsoidal-BGK (ES) and Shakhov (S) models, proposed in the late '60s by Holway [17] and Shakhov [18, 19], respectively. The accuracy of these models has been tested by considering the comparison to experimental [20, 21, 22] or DSMC [23, 24, 25] results. In the following, we refer to these two models (the ES and S models) as *the model equations*.

Various methods have been developed over the years to solve the model equations. Amongst these, we mention the discrete velocity method (DVM) [2, 26, 27, 28], the discrete unified gas kinetic scheme (DUGKS) [29, 30, 31], the discrete Boltzmann method [32, 33, 34, 35] and the lattice Boltzmann (LB) method [36, 37, 38, 39] and its finite difference (FDLB) version [23, 40, 41, 42, 43].

In the LB approach, the kinetic equation is employed to obtain an accurate account of the properties of the macroscopic moments of  $f$  [44, 45, 46, 47]. Less attention is directed to the distribution itself. This allows the momentum

space to be sampled in a manner optimized for the recovery of the moments of  $f$  [48]. Since the moments are defined as integrals of  $f$ , the momentum space discretization can be viewed as a quadrature method [41]. Our implementation is based on the idea of Gauss quadratures [49, 50], which provide a prescription of choosing optimal quadrature points for the recovery of polynomial integrals, given a certain domain and integration weight.

In this paper, we consider the systematic comparison between the numerical solutions of the Boltzmann equation with the S and ES models for the collision term, obtained using the FDLB algorithm, and the numerical results obtained using DSMC. The comparison is made in the frame of channel flows between parallel plates, where the fluid is assumed to be homogeneous with respect to the directions parallel to the plates. Specifically, we address three flow problems. The first one is the heat transfer between stationary plates at differing temperatures. The second is the Couette flow between parallel plates at equal temperatures. The third problem refers to the heat transfer between plates at differing temperatures undergoing parallel motion.

In channel flows, it is known that the particle-wall interaction induces a discontinuity in the distribution function [3, 51]. This discontinuity is responsible for microfluidics effects, such as the development of a slip velocity and temperature jump near the walls. Another important consequence of the discontinuity of  $f$  is that the velocity profile becomes non-analytic in the vicinity of the wall, where its derivative diverges logarithmically with respect to the distance to the wall [3, 52, 53].

As highlighted already in the late '50s by Gross and his collaborators [51, 54, 55, 56], taking into account the discontinuity of the distribution function by considering separately its moments with respect to the vectors pointing towards and away from the wall ( $p_x > 0$  and  $p_x < 0$ , respectively) can give a dramatic increase in the accuracy of the Knudsen layer representation, compared to the full momentum space projection approach. Recent works have focused on employing half-range quadratures [57, 58, 59] for the (semi-)analytical analysis of the solutions of the (linearized or non-linear) Boltzmann equation in the relaxation

time approximation,

An important step in employing the idea of treating separately the distribution function for incoming and outgoing particles with respect to solid walls in the numerical simulation of rarefied gas flows was taken in the '60s by Huang and Giddens [60], who computed the quadrature points and weights for the one-dimensional half-range Gauss-Hermite quadrature with the weight function  $\omega(x) = e^{-x^2}$ , up to 8th order. The extension of the procedure to higher orders through a recurrence relation was discussed by Ball in Ref. [61] and the algorithm was adapted in Ref. [43] to the case of the weight function  $\omega(x) = e^{-x^2/2}/\sqrt{2\pi}$ . A half-range (or modified) Gauss-Hermite quadrature was used in the early 2000's by Li and his collaborators [33, 62] for kinetic theory simulations in the context of unbounded flows. Recently, the half-range Gauss-Hermite quadrature was shown to offer significantly more accurate solutions of the kinetic model equations than the full-range Gauss-Hermite quadrature with the same number of quadrature points for the moderate and highly rarefied regimes [42, 43, 63]. As a side note, similarly accurate results can be obtained when the Gauss-Laguerre quadrature is used on the semi-axis, instead of the Gauss-Hermite quadrature [64, 65].

In order to take advantage of the geometry of the channel flows considered in this paper, we employ the mixed quadratures concept, according to which the quadrature is controlled separately on each axis [43, 58]. This approach allows the half-range Gauss-Hermite quadrature to be employed on the  $x$  axis, which is perpendicular to the channel walls. On the axes parallel to the walls, the full-range Gauss-Hermite quadrature can be employed. Details regarding Gauss quadratures can be found in various textbooks, of which we remind Refs. [49, 50].

Furthermore, in the channel flows considered in this paper, the dynamics is non-trivial only along  $d < D$  degrees of freedom (DOFs), where  $D = 3$  is the number of DOFs for an ideal monatomic gas. In particular, we consider  $d = 1$  when the walls are stationary and  $d = 2$  when the plates are in motion. We then introduce two reduced distributions,  $\phi$  and  $\chi$ , which are obtained integrating the distribution function  $f$  multiplied by 1 and  $[p_{d+1}^2 + \dots p_D^2]/m$

with respect to  $dp^{d+1} \dots dp^D$  [22]. Thus,  $\phi$  can be seen to describe the mass and momentum evolution and  $\chi$  contributes to the energy evolution [25]. When  $d = 2$ , we employ the mixed quadrature paradigm [43, 57] and discretize the momentum along the direction parallel to the wall using the full range Gauss-Hermite quadrature. Furthermore, the homogeneity of the fluid along these directions allows the system to be exactly described (i.e., without introducing any errors) using a relatively low order quadrature [25, 43]. In this paper, we introduce a novel expansion of the Shakhov and ellipsoidal collision terms which allows the quadrature orders along the  $y$  axis (which is parallel to the walls) to  $Q_y^\phi = 4$  and  $Q_y^\chi = 2$  for the  $\phi$  and  $\chi$  distributions, respectively.

For the analysis presented in this paper, only the stationary state is of interest. Since the transient solution is not important, iterative schemes can be employed to solve the kinetic model equation, as described, e.g., in Refs. [66, 67, 68]. However, since the computations in the one-dimensional settings that we consider in this paper are not very demanding, we compute the stationary solution using explicit time marching, implemented using the third order total variation diminishing Runge-Kutta (RK-3) method introduced in Refs. [69, 70, 71]. For the advection operator, we introduce a third order upwind scheme which preserves the order of accuracy in the presence of diffuse reflecting boundaries which extends the one considered in Ref. [72] for the linearised Boltzmann-BGK. We further increase the resolution inside the Knudsen layer by employing a grid stretching procedure [73, 74, 75] For simplicity, in this paper we only consider the Maxwell diffuse reflection model with complete accommodation at the bounding walls. The methodology can easily be extended to the case of more complex boundary conditions, such as the diffuse-specular [27] and the Cercignani-Lampis [76] boundary models.

This paper is organised as follows. The kinetic models and the connection to the DSMC simulations via the transport coefficients is presented in Sec. 2. The FDLB algorithm is summarized in Sec. 3 and the simulation methodology employed in the frame of the LB and DSMC approaches is summarized in Sec. 4. Sections 5, 6 and 7 present the numerical results for the heat transfer between

stationary plates, the Couette flow and the heat transfer between moving plates problems, respectively. Section 8 concludes this paper.

## 2. Kinetic models and connection to DSMC

Subsection 2.1 introduces briefly the Shakhov model, as well as the ellipsoidal-BGK model. Subsection 2.2 introduces the reduced distribution functions employed in the context of the channel flows discussed in this paper. The implementation of the transport coefficients using the numerical data obtained from *ab initio* potentials at the level of the model equations is discussed in Subsec. 2.3. Finally, our non-dimensionalization conventions are summarized in Subsec. 2.4.

### 2.1. Model equations in the relaxation time approximation

In this paper, we focus on the study of channel flows between parallel plates. The coordinate system is chosen such that the  $\tilde{x}$  axis is perpendicular to the walls. The discussion in this section is presented at the level of dimensional quantities, which are denoted explicitly via an overhead tilde. The origin of the coordinate system is taken to be on the channel centerline, such that the left and right walls are located at  $\tilde{x} = -\tilde{L}/2$  and  $\tilde{x} = \tilde{L}/2$ , respectively. The flow is studied in the Galilean frame where the left and right plates move with velocities  $-\tilde{u}_w$  and  $\tilde{u}_w$ , respectively ( $\tilde{u}_w = 0$  for the heat transfer problem between stationary plates discussed in Sec. 5). The temperatures of the left and right plates are set to  $\tilde{T}_{\text{left}} = \tilde{T}_{\text{ref}} - \widetilde{\Delta T}/2$  and  $\tilde{T}_{\text{right}} = \tilde{T}_{\text{ref}} + \widetilde{\Delta T}/2$ , respectively ( $\widetilde{\Delta T} = 0$  for the Couette flow problem discussed in Sec. 6). In this case, the Boltzmann equation in the relaxation time approximation for the collision term can be written as follows:

$$\frac{\partial \tilde{f}}{\partial t} + \frac{\tilde{p}_x}{\tilde{m}} \frac{\partial \tilde{f}}{\partial \tilde{x}} = -\frac{1}{\tilde{\tau}_*} (\tilde{f} - \tilde{f}_*), \quad (1)$$

where  $\tilde{f}$  is the particle distribution function,  $\tilde{p}_x$  is the particle momentum along the direction perpendicular to the walls,  $\tilde{m}$  is the particle mass and  $\tilde{\tau}_*$  is the relaxation time. The collision term governs the relaxation of  $\tilde{f}$  towards the local

equilibrium distribution function  $\tilde{f}_*$ . The star subscript in Eq. (1) distinguishes between the two models that we consider in this paper, namely the Shakhov model ( $* = S$ ) and the ellipsoidal-BGK ( $* = ES$ ) model. We consider in this paper only monatomic ideal gases, for which  $\tilde{f}_*$  reduces at global thermodynamic equilibrium to the Maxwell-Boltzmann distribution function  $\tilde{f}_{\text{MB}}$ :

$$\begin{aligned}\tilde{f}_{\text{MB}}(\tilde{n}, \tilde{\mathbf{u}}, \tilde{T}) &= \tilde{n} \tilde{g}(\tilde{p}_x, \tilde{u}_x, \tilde{T}) \tilde{g}(\tilde{p}_y, \tilde{u}_y, \tilde{T}) \tilde{g}(\tilde{p}_z, \tilde{u}_z, \tilde{T}), \\ \tilde{g}(\tilde{p}, \tilde{u}, \tilde{T}) &= \frac{1}{\sqrt{2\pi\tilde{m}\tilde{K}_B\tilde{T}}} \exp\left[-\frac{(\tilde{p} - \tilde{m}\tilde{u})^2}{2\tilde{m}\tilde{K}_B\tilde{T}}\right].\end{aligned}\quad (2)$$

Here  $\tilde{n}$  is the particle number density,  $\tilde{T}$  is the temperature and  $\tilde{u}_\alpha$  ( $\alpha \in \{x, y, z\}$ ) are the components of the macroscopic velocity. These quantities are obtained as moments of  $\tilde{f}$  and  $\tilde{f}_*$  via the following relations:

$$\begin{pmatrix} \tilde{n} \\ \tilde{\rho}\tilde{\mathbf{u}} \\ \frac{3}{2}\tilde{n}\tilde{K}_B\tilde{T} \end{pmatrix} = \int d^3\tilde{p} \begin{pmatrix} 1 \\ \tilde{\mathbf{p}} \\ \tilde{\xi}^2/2\tilde{m} \end{pmatrix} \tilde{f} = \int d^3\tilde{p} \begin{pmatrix} 1 \\ \tilde{\mathbf{p}} \\ \tilde{\xi}^2/2\tilde{m} \end{pmatrix} \tilde{f}_{\text{MB}}, \quad (3)$$

where  $\tilde{\xi} = \tilde{\mathbf{p}} - \tilde{m}\tilde{\mathbf{u}}$  is the peculiar momentum. The last equality above is a statement that the model equations preserve the collision invariants,  $\psi \in \{1, \mathbf{p}, \mathbf{p}^2/2m\}$ .

In the case of the Shakhov (S) model, the local equilibrium can be written as [18, 19, 23, 25, 77]:

$$\tilde{f}_S = \tilde{f}_{\text{MB}}(1 + \mathbb{S}), \quad \mathbb{S} = \frac{1 - \text{Pr}}{\tilde{n}\tilde{K}_B^2\tilde{T}^2} \left( \frac{\tilde{\xi}^2}{5\tilde{m}\tilde{K}_B\tilde{T}} - 1 \right) \tilde{\mathbf{q}} \cdot \tilde{\xi}, \quad (4)$$

where the heat flux  $\tilde{\mathbf{q}}$  is obtained via

$$\tilde{\mathbf{q}} = \int d^3\tilde{p} \tilde{f} \frac{\tilde{\xi}^2}{2\tilde{m}} \frac{\tilde{\xi}}{\tilde{m}}. \quad (5)$$

In the S model, the dynamic viscosity and the heat conductivity are controlled by the relaxation time  $\tilde{\tau}_S$  and the Prandtl number  $\text{Pr}$  through

$$\tilde{\mu}_S = \tilde{\tau}_S \tilde{P}, \quad \tilde{\kappa}_S = \frac{\tilde{c}_p \tilde{\mu}_S}{\text{Pr}} = \frac{5\tilde{K}_B \tilde{\tau}_S \tilde{P}}{2\tilde{m} \text{Pr}}, \quad (6)$$

where  $\tilde{c}_p = 5\tilde{K}_B/2\tilde{m}$  is the specific heat at constant pressure for an ideal monatomic gas.

In the ellipsoidal-BGK (ES) model, the equilibrium distribution  $\tilde{f}_{\text{ES}}$  can be written as [17, 24, 27, 35]:

$$\tilde{f}_{\text{ES}} = \frac{\tilde{n}}{(2\pi\tilde{m}\tilde{K}_B\tilde{T})^{3/2}\sqrt{\det\mathbb{B}}} \exp\left(-\frac{\mathbb{B}_{\alpha\beta}^{-1}\tilde{\xi}_\alpha\tilde{\xi}_\beta}{2\tilde{m}\tilde{K}_B\tilde{T}}\right), \quad (7)$$

where  $\mathbb{B}$  is an invertible  $3 \times 3$  matrix ( $1 \leq \alpha, \beta \leq D = 3$ ) having the following components:

$$\mathbb{B}_{\alpha\beta} = \frac{1}{\text{Pr}} \left[ \delta_{\alpha\beta} + (1 - \text{Pr}) \frac{\tilde{T}_{\alpha\beta}}{\tilde{P}} \right]. \quad (8)$$

In the above,  $\tilde{P} = \tilde{n}\tilde{K}_B\tilde{T}$  is the ideal gas pressure, while the Cartesian components  $\tilde{T}_{\alpha\beta}$  of the pressure tensor are obtained as second order moments of  $\tilde{f}$ :

$$\tilde{T}_{\alpha\beta} = \int d^3\tilde{p} \tilde{f} \frac{\tilde{\xi}_\alpha\tilde{\xi}_\beta}{\tilde{m}}. \quad (9)$$

In the ES model, the transport coefficients are retrieved through:

$$\tilde{\mu}_{\text{ES}} = \tilde{\tau}_{\text{ES}} \text{Pr} \tilde{P}, \quad \tilde{\kappa}_{\text{ES}} = \frac{\tilde{c}_p \tilde{\mu}_{\text{ES}}}{\text{Pr}} = \frac{5\tilde{K}_B\tilde{\tau}_{\text{ES}}\tilde{P}}{2\tilde{m}}. \quad (10)$$

The equation (1) is supplemented by boundary conditions. In this paper, we restrict the analysis to the case of diffuse reflection with complete accommodation, such that the distribution of the particles emerging from the wall back into the fluid is described by the Maxwell-Boltzmann distribution [27]:

$$\begin{aligned} \tilde{f}(-\tilde{L}/2, \tilde{p}_x > 0, \tilde{t}) &= \tilde{f}_{\text{MB}}(\tilde{n}_{\text{left}}, -\tilde{\mathbf{u}}_w, \tilde{T}_{\text{left}}), \\ \tilde{f}(\tilde{L}/2, \tilde{p}_x < 0, \tilde{t}) &= \tilde{f}_{\text{MB}}(\tilde{n}_{\text{right}}, \tilde{\mathbf{u}}_w, \tilde{T}_{\text{right}}), \end{aligned} \quad (11)$$

where  $\tilde{n}_{\text{left}}$  and  $\tilde{n}_{\text{right}}$  are determined by imposing zero mass flux through the walls:

$$\int d^3\tilde{p} \tilde{f}(\pm\tilde{L}/2, \tilde{\mathbf{p}}, \tilde{t}) \tilde{p}_x = 0. \quad (12)$$

Substituting Eq. (11) into Eq. (12) gives [22]:

$$\begin{aligned} \tilde{n}_{\text{left}} &= -\sqrt{\frac{2\pi}{\tilde{m}\tilde{K}_B\tilde{T}_{\text{left}}}} \int_{\tilde{p}_x < 0} d^3\tilde{p} \tilde{f}(-\tilde{L}/2, \tilde{\mathbf{p}}, \tilde{t}) \tilde{p}_x, \\ \tilde{n}_{\text{right}} &= \sqrt{\frac{2\pi}{\tilde{m}\tilde{K}_B\tilde{T}_{\text{right}}}} \int_{\tilde{p}_x > 0} d^3\tilde{p} \tilde{f}(\tilde{L}/2, \tilde{\mathbf{p}}, \tilde{t}) \tilde{p}_x. \end{aligned} \quad (13)$$

## 2.2. Reduced distributions

In the context of the channel flows considered in this paper, the dynamics along the  $z$  direction is trivial. Moreover, in the heat transfer problem without shear, the dynamics along the  $y$  axis also becomes trivial. In this context, it is convenient to integrate out the trivial momentum space degrees of freedom at the level of the model equation.

For notational convenience, let  $D = 3$  represent the total number of degrees of freedom of the momentum space. Denoting by  $d$  the number of non-trivial momentum space degrees of freedom, the  $D - d$  degrees of freedom can be integrated out and two reduced distribution functions,  $\tilde{\phi}$  and  $\tilde{\chi}$ , can be introduced as follows [22, 62, 78]:

$$\tilde{\phi} = \int d^{D-d} \tilde{p} \tilde{f}, \quad \tilde{\chi} = \int d^{D-d} \tilde{p} \frac{\tilde{p}_{d+1}^2 + \dots + \tilde{p}_D^2}{\tilde{m}} \tilde{f}. \quad (14)$$

The evolution equations for  $\tilde{\phi}$  and  $\tilde{\chi}$  can be obtained by multiplying Eq. (1) with the appropriate factors and integrating with respect to the  $D - d$  trivial momentum space degrees of freedom:

$$\frac{\partial}{\partial t} \begin{pmatrix} \tilde{\phi} \\ \tilde{\chi} \end{pmatrix} + \frac{\tilde{p}_x}{\tilde{m}} \frac{\partial}{\partial \tilde{x}} \begin{pmatrix} \tilde{\phi} \\ \tilde{\chi} \end{pmatrix} = -\frac{1}{\tilde{\tau}_*} \begin{pmatrix} \tilde{\phi} - \tilde{\phi}_* \\ \tilde{\chi} - \tilde{\chi}_* \end{pmatrix}. \quad (15)$$

Denoting using latin indices  $i$  and  $j$  the components corresponding to the non-trivial directions ( $1 \leq i, j \leq d$ ), the macroscopic moments given in Eqs. (3), (9) and (5) can be obtained through:

$$\begin{pmatrix} \tilde{n} \\ \tilde{\rho} u_i \\ \tilde{T}_{ij} \end{pmatrix} = \int d^d \tilde{p} \begin{pmatrix} 1 \\ \tilde{p}_i \\ \tilde{\xi}_i \tilde{\xi}_j / \tilde{m} \end{pmatrix} \tilde{\phi},$$

$$\begin{pmatrix} \frac{3}{2} \tilde{n} \tilde{K}_B \tilde{T} \\ \tilde{q}_i \end{pmatrix} = \int d^d \tilde{p} \begin{pmatrix} 1 \\ \tilde{\xi}_i / \tilde{m} \end{pmatrix} \left( \frac{\tilde{\xi}_j \tilde{\xi}_j}{2\tilde{m}} \tilde{\phi} + \frac{1}{2} \tilde{\chi} \right), \quad (16)$$

where the summation over the repeated index  $j$  is implied.

For the Shakhov model,  $\tilde{\phi}_S$  and  $\tilde{\chi}_S$  are given by:

$$\begin{aligned}\tilde{\phi}_S &= \tilde{\phi}_{\text{MB}}(1 + \mathbb{S}_\phi), & \mathbb{S}_\phi &= \frac{1 - \text{Pr}}{(D+2)\tilde{n}\tilde{K}_B\tilde{T}^2} \left( \frac{\tilde{\xi}_j\tilde{\xi}_j}{\tilde{m}\tilde{K}_B\tilde{T}} - d - 2 \right) \tilde{q}_i\tilde{\xi}_i, \\ \tilde{\chi}_S &= (D-d)\tilde{K}_B\tilde{T}\tilde{\phi}_{\text{MB}}(1 + \mathbb{S}_\chi), & \mathbb{S}_\chi &= \frac{1 - \text{Pr}}{(D+2)\tilde{n}\tilde{K}_B\tilde{T}^2} \left( \frac{\tilde{\xi}_j\tilde{\xi}_j}{\tilde{m}\tilde{K}_B\tilde{T}} - d \right) \tilde{q}_i\tilde{\xi}_i,\end{aligned}\tag{17}$$

where the summation over the repeated index  $j$  is implied in the second and third lines. The reduced Maxwell-Boltzmann distribution  $\tilde{\phi}_{\text{MB}}$  is:

$$\tilde{\phi}_{\text{MB}} = \tilde{n}\tilde{g}_x(\tilde{p}_x, \tilde{u}_x, \tilde{T}) \cdots \tilde{g}_d(\tilde{p}_d, \tilde{u}_d, \tilde{T}).\tag{18}$$

Before discussing the ES model, we first mention that the representation as a  $D \times D$  matrix of the pressure tensor  $\tilde{T}_{\alpha\beta}$  admits the following block decomposition:

$$\tilde{T}_{\alpha\beta} = \begin{pmatrix} \tilde{T}_{ij} & 0_{ib} \\ 0_{aj} & \tilde{P}_{\text{red}}\delta_{ab} \end{pmatrix},\tag{19}$$

where the latin indices at the beginning of the alphabet run over the trivial degrees of freedom, i.e.  $d < a, b \leq D$ . With this convention, the top left and bottom right blocks are  $d \times d$  and  $(D-d) \times (D-d)$  matrices with components  $\tilde{T}_{ij}$  and  $\tilde{P}_{\text{red}}\delta_{ab}$ , respectively, while the top right and bottom left blocks are  $d \times (D-d)$  and  $(D-d) \times d$  null matrices, respectively. The Kronecker delta  $\delta_{ab}$  takes the value 1 when  $a = b$  and 0 otherwise. The scalar quantity  $\tilde{P}_{\text{red}}$  is obtained from Eq. (16):

$$\tilde{P}_{\text{red}} = \frac{D\tilde{P} - \sum_{j=1}^d \tilde{T}_{jj}}{D-d}.\tag{20}$$

Using the same decomposition as in Eq. (19), the matrix  $\mathbb{B}_{\alpha\beta}$  can be written as:

$$\mathbb{B}_{\alpha\beta} = \begin{pmatrix} \mathcal{B}_{ij} & 0 \\ 0 & \mathbb{B}_{\text{red}}\delta_{\alpha\beta} \end{pmatrix},\tag{21}$$

where

$$\mathcal{B}_{ij} = \frac{1}{\text{Pr}}\delta_{ij} - \frac{1 - \text{Pr}}{\text{Pr}} \frac{\tilde{T}_{ij}}{\tilde{P}}.\tag{22}$$

The scalar quantity  $\mathbb{B}_{\text{red}}$  is given by:

$$\mathbb{B}_{\text{red}} = \frac{1}{\text{Pr}} - \frac{1 - \text{Pr}}{\text{Pr}} \frac{\tilde{P}_{\text{red}}}{\tilde{P}}. \quad (23)$$

It can be seen that the determinant of  $\mathbb{B}$  can be written as:

$$\det \mathbb{B} = \mathbb{B}_{\text{red}}^{D-d} \det \mathcal{B}. \quad (24)$$

This allows the integral of  $\tilde{f}_{\text{ES}}$  over the  $D - d$  trivial degrees of freedom to be performed analytically, giving:

$$\tilde{\phi}_{\text{ES}} = \frac{\tilde{n}}{(2\pi\tilde{m}\tilde{K}_B\tilde{T})^{d/2}\sqrt{\det \mathcal{B}}} \exp\left(-\frac{\mathcal{B}_{ij}^{-1}\tilde{\xi}_i\tilde{\xi}_j}{2\tilde{m}\tilde{K}_B\tilde{T}}\right), \quad (25)$$

while  $\tilde{\chi}_{\text{ES}} = (D - d)\tilde{K}_B\tilde{T}_{\text{red}}\tilde{\phi}_{\text{ES}}$  and  $\tilde{K}_B\tilde{T}_{\text{red}} = \tilde{P}_{\text{red}}/\tilde{n}$ .

### 2.3. *Ab initio* transport coefficients

In this paper, we consider a series of comparisons between the results obtained in the frame of the model equations introduced in the previous subsections and the results obtained using the DSMC method with *ab initio* particle interactions. The connection between these two formulations can be made at the level of the transport coefficients. The basis for the approach that we take in this paper is to note that in the variable hard spheres model, the viscosity has a temperature dependence of the form [5]

$$\tilde{\mu} = \tilde{\mu}_{\text{ref}}(\tilde{T}/\tilde{T}_{\text{ref}})^\omega, \quad (26)$$

where the tilde denotes dimensionful quantities, as discussed in the previous subsection. The viscosity index  $\omega$  introduced above takes the values 1/2 and 1 for hard sphere and Maxwell molecules, respectively. For real gases,  $\omega$  is in general temperature-dependent. This temperature dependence is not known analytically, however the values of  $\tilde{\mu}$  and  $\tilde{\kappa}$  corresponding to a gas comprised of molecules interacting via *ab initio* potentials can be computed numerically. The supplementary material in Ref. [79] contains the data corresponding to  $^3\text{He}$  and  $^4\text{He}$  constituents in the temperature range  $1 \text{ K} \leq \tilde{T} \leq 10000 \text{ K}$ , while

the data for Ne covering the range  $20 \text{ K} \leq \tilde{T} \leq 10000 \text{ K}$  can be found in the tables reported in Ref. [80]. In order to perform simulations of the heat transfer problem (discussed in Sec. 7) at  $\tilde{T}_{\text{ref}} = 1 \text{ K}$  (for He constituents) and  $20 \text{ K}$  (for Ne constituents), we require data for the transport coefficients in the temperature range  $0.25 \text{ K} \leq \tilde{T} \leq 1 \text{ K}$  and  $5 \text{ K} \leq \tilde{T} \leq 20 \text{ K}$ , respectively. These data were obtained by the method described in Ref. [80].

The temperature dependence of the viscosity index  $\omega$  is accounted for by employing Eq. (26) in a piecewise fashion. Let  $n$  ( $1 \leq n \leq N$ ) represent the index of the tabulated values  $\tilde{T}_1 < \tilde{T}_2 < \dots < \tilde{T}_N$  of the temperature, where  $N$  is the total number of available entries. Considering a temperature interval  $\tilde{T}_n \leq \tilde{T} \leq \tilde{T}_{n+1}$ , we define

$$\tilde{\mu}^{(n)}(\tilde{T}) = \tilde{\mu}_n \left( \frac{\tilde{T}}{\tilde{T}_n} \right)^{\omega_n}, \quad \omega_n = \frac{\ln(\tilde{\mu}_{n+1}/\tilde{\mu}_n)}{\ln(\tilde{T}_{n+1}/\tilde{T}_n)}, \quad (27)$$

where  $\tilde{\mu}_n$  and  $\tilde{\mu}_{n+1}$  are the tabulated values of the viscosity corresponding to the temperatures  $\tilde{T}_n$  and  $\tilde{T}_{n+1}$ , respectively. The above formula ensures that the function  $\tilde{\mu}^{(n)}$  satisfies  $\tilde{\mu}^{(n)}(\tilde{T}_n) = \tilde{\mu}_n$  and  $\tilde{\mu}^{(n)}(\tilde{T}_{n+1}) = \tilde{\mu}_{n+1}$ .

The Prandtl number  $\text{Pr}$  is also defined in a piecewise fashion. For the temperature range  $\tilde{T}_n \leq \tilde{T} < \tilde{T}_{n+1}$ , we define  $\text{Pr}_n$  as

$$\text{Pr}_n = \frac{\tilde{c}_p \tilde{\mu}_n}{\tilde{\kappa}_n}, \quad (28)$$

where  $\tilde{\kappa}_n$  is the heat conductivity corresponding to the temperature  $\tilde{T} = \tilde{T}_n$ , retrieved from the tabulated data mentioned above.

In general, the temperatures encountered in our simulations are within the bounds of the temperature range for which data is available for interpolation. For completeness, we present a possible extension of the above procedure for values of the temperature which are outside the range spanned by the tabulated data. In the case when  $\tilde{T} < \tilde{T}_2$ , we propose to use  $\tilde{\mu}(\tilde{T}) = \tilde{\mu}^{(1)}(\tilde{T})$  and  $\text{Pr}(\tilde{T}) = \text{Pr}_1$ . For  $\tilde{T} > \tilde{T}_N$ , where  $\tilde{T}_N$  is the highest available temperature in the tabulated data, we propose to use  $\tilde{\mu}(\tilde{T}) = \tilde{\mu}^{(N-1)}(\tilde{T})$  and  $\text{Pr}(\tilde{T}) = \text{Pr}_N$ .

The algorithm described in this section can be summarized through [77]:

$$\begin{aligned} \tilde{\mu}(\tilde{T}) &= \begin{cases} \tilde{\mu}^{(1)}(\tilde{T}), & \tilde{T} < \tilde{T}_2, \\ \tilde{\mu}^{(n)}(\tilde{T}), & \tilde{T}_n < \tilde{T} < \tilde{T}_{n+1}, \\ \tilde{\mu}^{(N-1)}(\tilde{T}), & \tilde{T}_N < \tilde{T}, \end{cases} \\ \text{Pr}(\tilde{T}) &= \begin{cases} \text{Pr}_1, & \tilde{T} < \tilde{T}_2, \\ \text{Pr}_n, & \tilde{T}_n < \tilde{T} < \tilde{T}_{n+1}, \\ \text{Pr}_N, & \tilde{T}_N < \tilde{T}, \end{cases} \end{aligned} \quad (29)$$

where  $n = 2, 3, \dots, N - 1$  refers to the index of the tabulated data.

#### 2.4. Non-dimensionalization convention

All simulation results reported in this paper are based on the nondimensionalization conventions employed in Ref. [25], which are summarized here for completeness. In general, the dimensionless form  $A$  of a dimensional quantity  $\tilde{A}$  is obtained by dividing the latter with respect to its reference value,  $\tilde{A}_{\text{ref}}$ :

$$A = \frac{\tilde{A}}{\tilde{A}_{\text{ref}}}. \quad (30)$$

We employ the convention that dimensionless quantities are denoted without the overhead tilde encountered for their dimensionful counterparts. The reference temperature is taken as the average of the wall temperatures:

$$\tilde{T}_{\text{ref}} = \frac{\tilde{T}_{\text{left}} + \tilde{T}_{\text{right}}}{2}. \quad (31)$$

The reference speed is defined through:

$$\tilde{c}_{\text{ref}} = \sqrt{\frac{\tilde{K}_B \tilde{T}_{\text{ref}}}{\tilde{m}}}, \quad (32)$$

where the particle mass  $\tilde{m}$  takes the values  $5.0082373 \times 10^{-27}$  kg,  $6.6464764 \times 10^{-27}$  kg, and  $3.3509177 \times 10^{-26}$  kg for  $^3\text{He}$ ,  $^4\text{He}$ , and Ne, respectively.

The reference particle number density is taken as the average particle number density over the channel:

$$\tilde{n}_{\text{ref}} = \frac{1}{\tilde{L}} \int_{-\tilde{L}/2}^{\tilde{L}/2} d\tilde{x} \tilde{n}. \quad (33)$$

The reference length is taken to be the channel width:

$$\tilde{L}_{\text{ref}} = \tilde{L}. \quad (34)$$

Finally, the reference time is

$$\tilde{t}_{\text{ref}} = \frac{\tilde{L}_{\text{ref}}}{\tilde{c}_{\text{ref}}} = \tilde{L} \sqrt{\frac{\tilde{m}}{\tilde{K}_B \tilde{T}_{\text{ref}}}}. \quad (35)$$

The dimensionless relaxation time  $\tau_* = \tilde{\tau}_*/\tilde{t}_{\text{ref}}$  in the S and ES models becomes:

$$\tau_S = \frac{\mu(T)}{P\delta\sqrt{2}}, \quad \tau_{\text{ES}} = \frac{\mu(T)}{P_{\text{r}}P\delta\sqrt{2}}, \quad (36)$$

where the rarefaction parameter  $\delta$  is defined through [10]:

$$\delta = \frac{\tilde{L}\tilde{P}_{\text{ref}}}{\tilde{\mu}_{\text{ref}}\tilde{c}_{\text{ref}}\sqrt{2}}, \quad (37)$$

In the above,  $\tilde{\mu}_{\text{ref}} = \tilde{\mu}(\tilde{T}_{\text{ref}})$  and  $\tilde{P}_{\text{ref}} = \tilde{n}_{\text{ref}}\tilde{K}_B\tilde{T}_{\text{ref}}$ .

The distribution function  $\tilde{f}$  is nondimensionalized via

$$f = \frac{\tilde{f}\tilde{P}_{\text{ref}}^D}{\tilde{n}_{\text{ref}}}, \quad (38)$$

where  $\tilde{p}_{\text{ref}} = \sqrt{\tilde{m}\tilde{K}_B\tilde{T}_{\text{ref}}}$ . The reduced distributions can be nondimensionalized in a similar fashion:

$$\phi = \frac{\tilde{\phi}\tilde{p}_{\text{ref}}^d}{\tilde{n}_{\text{ref}}}, \quad \chi = \frac{\tilde{\chi}\tilde{p}_{\text{ref}}^d}{\tilde{P}_{\text{ref}}}. \quad (39)$$

This allows Eq. (15) to be written as:

$$\frac{\partial}{\partial t} \begin{pmatrix} \phi \\ \chi \end{pmatrix} + \frac{p_x}{m} \frac{\partial}{\partial x} \begin{pmatrix} \phi \\ \chi \end{pmatrix} = -\frac{1}{\tau_*} \begin{pmatrix} \phi - \phi_* \\ \chi - \chi_* \end{pmatrix}. \quad (40)$$

### 3. Mixed quadrature lattice Boltzmann models

In this section, the LB algorithm employed to solve Eq. (40) is briefly described. There are three pieces to the algorithm, which will be described in the following subsections. The first concerns the implementation of both the time stepping and the advection, which will be addressed in Subsec. 3.1. The second concerns the discretization of the momentum space using the full-range and

half-range Gauss-Hermite quadratures. This will be discussed in Subsec. 3.2. The third and final piece is the projection of the collision term in the model equation on the space generated by the full-range (for the directions parallel to the wall) and half-range (for the direction perpendicular to the walls) Hermite polynomials. Details will be given in Subsec. 3.3.

### 3.1. Time stepping and advection

In order to describe the time stepping algorithm, Eq. (15) is written as:

$$\partial_t F = L[F], \quad (41)$$

where  $F \in \{\phi, \chi\}$  represents the reduced distributions. Considering the equidistant discretization of the time variable using intervals  $\delta t$  and using  $t_n = n\delta t$  to denote the time coordinate after  $n$  iterations, we employ the third order total variation diminishing Runge-Kutta scheme to obtain the  $F_{n+1}$  at time  $t_{n+1}$  through two intermediate steps [69, 70, 71]:

$$\begin{aligned} F_n^{(1)} &= F_n + \delta t L[F_n], \\ F_n^{(2)} &= \frac{3}{4}F_n + \frac{1}{4}F_n^{(1)} + \frac{1}{4}\delta t L[F_n^{(1)}], \\ F_{n+1} &= \frac{1}{3}F_n + \frac{2}{3}F_n^{(2)} + \frac{2}{3}\delta t L[F_n^{(2)}]. \end{aligned} \quad (42)$$

As pointed out by various authors [73, 74, 75], an accurate account for the Knudsen layer phenomena requires a sufficiently fine grid close to the wall. This can be achieved by performing a coordinate change from  $x = \tilde{x}/\tilde{L}$  to the coordinate  $\eta$ , defined through [25, 75, 77, 81]:

$$x = \frac{\tanh \eta}{2A}, \quad (43)$$

where the stretching parameter  $A$  controls the grid refinement. When  $A \rightarrow 0$ , the grid becomes equidistant, while as  $A \rightarrow 1$ , the grid points accumulate towards the boundaries at  $x = \pm 1/2$ . The channel walls are located at  $\eta = \pm \arctan A$ .

The  $\eta$  coordinate is discretized symmetrically with respect to the channel centerline (where  $x = 0$  and  $\eta = 0$ ). On the right half of the channel,  $S$

equidistant intervals of size  $\delta\eta = \operatorname{arctanh} A/S$  are employed. In the case of the Couette flow, which is symmetric with respect to the channel centerline, the simulation setup contains only the domain  $0 \leq \eta \leq A$  and the total number of grid points is equal to  $S$  [25, 81]. The center of cell  $s$  ( $1 \leq s \leq S$  for the right half of the channel and  $-S < s \leq 0$  for its left half) is located at  $\eta_s = (s - \frac{1}{2})\delta\eta$ . At each node  $s$ , the advection term is computed using the third order upwind (U3) method, implemented using a flux-based approach:

$$\left(\frac{p_x}{m} \frac{\partial F}{\partial x}\right)_s = \frac{p_x}{m} \left(\frac{\partial \eta}{\partial x}\right)_s \left(\frac{\partial F}{\partial \eta}\right)_s = 2A \cosh^2 \eta_s \frac{\mathcal{F}_{s+1/2} - \mathcal{F}_{s-1/2}}{\delta\eta} + O(\delta\eta^3). \quad (44)$$

The stencil employed for the flux  $\mathcal{F}_{s+1/2}$  is chosen depending on the sign of the advection velocity  $p_x/m$ :

$$\mathcal{F}_{s+1/2} = \frac{p_x}{m} \begin{cases} \frac{1}{3}F_{s+1} + \frac{5}{6}F_s - \frac{1}{6}F_{s-1}, & p_x > 0, \\ \frac{1}{3}F_s + \frac{5}{6}F_{s+1} - \frac{1}{6}F_{s+2}, & p_x < 0. \end{cases} \quad (45)$$

The diffuse reflection boundary conditions in Eq. (11) specify the distributions  $\phi$  and  $\chi$  on the channel walls. For definiteness, we will refer to the right boundary, which is located at  $\eta_{S+1/2} = \operatorname{arctanh} A$ . In order to perform the advection at node  $S$  for the particles traveling towards the wall (having  $p_x > 0$ ), the value of the distribution function in the node  $s = S + 1$  is required. This value can be obtained using a third order extrapolation from the fluid nodes:

$$F_{S+1}^{p_x > 0} = 4F_S - 6F_{S-1} + 4F_{S-2} - F_{S-3}. \quad (46)$$

It can be shown that the third order accuracy in the sense of Eq. (44) is preserved when the fluxes  $\mathcal{F}_{S+1/2}$  and  $\mathcal{F}_{S-1/2}$  are computed using Eq. (45). For the particles traveling towards the fluid ( $p_x < 0$ ), the nodes at  $S + 1$  and  $S + 2$  must be populated. According to the diffuse reflection concept, summarized in Eq. (11), the reduced distributions at  $s = S + 1/2$  are set to:

$$\begin{aligned} \phi_{S+1/2} &= \phi_{\text{MB}}(n_{\text{right}}, \mathbf{u}_w, T_{\text{right}}), \\ \chi_{S+1/2} &= (D - d)T_{\text{right}}\phi_{S+1/2}, \end{aligned} \quad (47)$$

where  $T_{\text{right}} = 1 + \Delta T/2$  is the temperature on the right wall ( $\Delta T = 0$  in the case of Couette flow). The distributions in the ghost nodes at  $S + 1$  and  $S + 2$  can be set to [72]:

$$\begin{aligned} F_{S+1}^{p_x < 0} &= \frac{16}{5} F_{S+1/2} - 3F_S + F_{S-1} - \frac{1}{5} F_{S-2}, \\ F_{S+2}^{p_x < 0} &= 4F_{S+1} - 6F_S + 4F_{S-1} - F_{S-2}. \end{aligned} \quad (48)$$

The expression for  $F_{S+2}$  can be seen to represent a third order extrapolation from the nodes with  $S - 2 \leq s \leq S + 1$ . In the expression for  $F_{S+1}$ , the distribution at the wall,  $F_{S+1/2}$  is employed. It can be checked by direct substitution in Eq. (44) that the third order accuracy is preserved when the ghost nodes are populated as indicated above.

The density  $n_{\text{right}}$  in Eq. (47) can be computed using the discrete equivalent of Eq. (12):

$$\int d^d p \Phi_{S+1/2} = 0, \quad (49)$$

where  $\Phi_{S+1/2}$  is the flux corresponding to the reduced distribution  $\phi$ , computed using Eq. (45). Using Eq. (48), the flux for outgoing particles is:

$$\begin{aligned} \Phi_{S+1/2}^{p_x < 0} &= \frac{p_x}{m} \left( \frac{8}{15} \phi_{S+1/2} + \frac{5}{6} \phi_S - \frac{1}{2} \phi_{S-1} + \frac{2}{15} \phi_{S-2} \right), \\ \Phi_{S-1/2}^{p_x < 0} &= \frac{p_x}{m} \left( -\frac{8}{15} \phi_{S+1/2} + \frac{4}{3} \phi_S + \frac{1}{6} \phi_{S-1} + \frac{1}{30} \phi_{S-2} \right), \end{aligned} \quad (50)$$

where the flux  $\Phi_{S-1/2}$  is given above for completeness. Due to the above expression for  $\Phi_{S+1/2}^{p_x < 0}$ , it can be seen that the unknown density,  $n_{\text{right}}$ , enters Eq. (49) through the distribution  $\phi_{S+1/2}$ , which is fixed by boundary conditions for momenta pointing towards the fluid ( $p_x < 0$ ), according to Eq. (47). Splitting the integration domain in Eq. (49) in two domains, corresponding to positive and negative values of  $p_x$ , the integral for  $p_x < 0$  of  $\phi_{S+1/2}$  can be computed as follows:

$$\int_{p_x < 0} d^d p \frac{p_x}{m} \phi_{S+1/2} = -n_{\text{right}} \sqrt{\frac{T_{\text{right}}}{2\pi m}}. \quad (51)$$

Taking into account Eqs. (50) and (51), the following expression is obtained for

$n_{\text{right}}$ :

$$n_{\text{right}} = \frac{15}{8} \sqrt{\frac{2\pi m}{T_{\text{right}}}} \left[ \int_{p_x > 0} d^d p \Phi_{S+1/2} - \int_{p_x < 0} d^d p \frac{p_x}{m} \left( \frac{5}{6} \phi_S - \frac{1}{2} \phi_{S-1} + \frac{2}{15} \phi_{S-2} \right) \right]. \quad (52)$$

For completeness, we also give below the expressions for  $\Phi_{S+1/2}$  when  $p_x > 0$ :

$$\Phi_{S+1/2}^{p_x > 0} = \frac{p_x}{m} \left( \frac{13}{6} \phi_S - \frac{13}{6} \phi_{S-1} + \frac{4}{3} \phi_{S-2} - \frac{1}{3} \phi_{S-3} \right). \quad (53)$$

In the case of the Couette flow, only the nodes with  $1 \leq s \leq S$  comprise the fluid domain, while bounce-back boundary conditions are imposed on the channel centerline ( $s = 1/2$ ). The nodes with  $s < 1$  become ghost nodes, which are populated according to:

$$p_x < 0 : F_0(\mathbf{p}) = -F_1(-\mathbf{p}), \quad p_x > 0 : \begin{cases} F_0(\mathbf{p}) = -F_1(-\mathbf{p}), \\ F_{-1}(\mathbf{p}) = -F_2(-\mathbf{p}). \end{cases} \quad (54)$$

### 3.2. Momentum space discretization

Through the discretization of the momentum space, the integrals defining the macroscopic moments in Eq. (16) are replaced by quadrature sums, i.e.:

$$\begin{aligned} \begin{pmatrix} n \\ \rho u_i \\ T_{ij} \end{pmatrix} &\simeq \sum_{\boldsymbol{\kappa}} \begin{pmatrix} 1 \\ p_{\boldsymbol{\kappa};i} \\ \xi_{\boldsymbol{\kappa};i} \xi_{\boldsymbol{\kappa};j} / m \end{pmatrix} \phi_{\boldsymbol{\kappa}}, \\ \left( \frac{3}{2} n T \right) &\simeq \sum_{\boldsymbol{\kappa}} \begin{pmatrix} 1 \\ \xi_{\boldsymbol{\kappa};i} / m \end{pmatrix} \frac{\xi_{\boldsymbol{\kappa};j} \xi_{\boldsymbol{\kappa};j}}{2m} \phi_{\boldsymbol{\kappa}} + \frac{1}{2} \sum_{\boldsymbol{\sigma}} \begin{pmatrix} 1 \\ \xi_{\boldsymbol{\sigma};i} / m \end{pmatrix} \chi_{\boldsymbol{\sigma}}, \end{aligned} \quad (55)$$

where  $\boldsymbol{\kappa}$  and  $\boldsymbol{\sigma}$  collectively denote the indices labeling the momenta corresponding to the discrete populations  $\phi_{\boldsymbol{\kappa}}$  and  $\chi_{\boldsymbol{\sigma}}$ .

The discretization on the axis perpendicular to the walls (the  $x$  axis), is performed using the half-range Gauss-Hermite quadrature prescription [43]. While in principle,  $p_x$  can be discretized separately for the  $\phi$  and  $\chi$  distributions, for simplicity we consider the same quadrature order  $Q_x^\phi = Q_x^\chi \equiv Q_x$  on each  $x$

semiaxis throughout this paper. Focusing on the distribution  $\phi$ , the discrete momentum components  $p_{x,k_x}$  ( $1 \leq k_x \leq 2Q_x$ ) are linked to the roots of the half-range Hermite polynomial  $\mathfrak{h}_{Q_x}(z)$  of order  $Q_x$  via:

$$p_{x,k_x} = \begin{cases} p_{0,x} z_{k_x}, & 1 \leq k_x \leq Q_x, \\ -p_{0,x} z_{k_x - Q_x}, & Q_x < k_x \leq 2Q_x, \end{cases} \quad (56)$$

where  $\mathfrak{h}_{Q_x}(z_{k_x}) = 0$  for  $1 \leq k_x \leq Q_x$ , while  $p_{0,x}$  represents a constant momentum scale (we set  $p_{0,x} = 1$  in the rest of this paper). The same considerations apply for the distribution  $\chi$ , after replacing  $k_x$  with the index  $s_x$  ( $1 \leq s_x \leq 2Q_x$ ).

When  $d = 1$ , the populations  $\phi_{\kappa} \equiv \phi_{k_x}$  and  $\chi_{\sigma} \equiv \chi_{s_x}$  are linked to the continuum distributions  $\phi$  and  $\chi$  through:

$$\phi_{k_x} = \frac{p_{0,x} w_{k_x}^{\mathfrak{h}}(Q_x)}{\omega(\bar{p}_{x,k_x})} \phi(\bar{p}_{x,k_x}), \quad \chi_{s_x} = \frac{p_{0,x} w_{s_x}^{\mathfrak{h}}(Q_x)}{\omega(\bar{p}_{x,s_x})} \chi(\bar{p}_{x,s_x}), \quad (57)$$

where the weight function  $\omega(z)$  is defined through:

$$\omega(z) = \frac{1}{\sqrt{2\pi}} e^{-z^2/2}. \quad (58)$$

The quadrature weights  $w_k^{\mathfrak{h}}(Q)$  can be computed using [43, 82]

$$\begin{aligned} w_k^{\mathfrak{h}}(Q) &= \frac{\bar{p}_{x,k} a_Q^2}{\mathfrak{h}_{Q+1}^2(\bar{p}_{x,k}) [\bar{p}_{x,k} + \mathfrak{h}_Q^2(0)/\sqrt{2\pi}]} \\ &= \frac{\bar{p}_{x,k} a_{Q-1}^2}{\mathfrak{h}_{Q-1}^2(\bar{p}_{x,k}) [\bar{p}_{x,k} + \mathfrak{h}_Q^2(0)/\sqrt{2\pi}]}. \end{aligned} \quad (59)$$

In the above,  $a_Q = \mathfrak{h}_{Q+1,Q+1}/\mathfrak{h}_{Q,Q}$  represents the ratio of the coefficients of the leading power of  $\bar{p}_x$  in  $\mathfrak{h}_{Q+1}(\bar{p}_x)$  and  $\mathfrak{h}_Q(\bar{p}_x)$ . Specifically, the notation  $\mathfrak{h}_{\ell,s}$  refers to the coefficient of  $x^s$  appearing in  $\mathfrak{h}_{\ell}(\bar{p}_x)$ , namely:

$$\mathfrak{h}_{\ell}(\bar{p}_x) = \sum_{s=0}^{\ell} \mathfrak{h}_{\ell,s} \bar{p}_x^s. \quad (60)$$

In the case when the boundaries are moving,  $d = 2$  and the momentum component  $p_y$  is discretized using the full-range Gauss-Hermite quadrature prescription. As remarked in Refs. [43, 25], a small order quadrature is sufficient to ensure the exact recovery of the dynamics along this axis. To assess the

quadrature orders for the  $\phi$  and  $\chi$  distributions, we consider the expansions of  $\phi$  and  $\chi$  with respect to the full-range Hermite polynomials for the  $p_y$  degree of freedom:

$$\begin{pmatrix} \phi \\ \chi \end{pmatrix} = \frac{\omega(\bar{p}_y)}{p_{0;y}} \sum_{\ell=0}^{\infty} \frac{1}{\ell!} H_{\ell}(\bar{p}_y) \begin{pmatrix} \Phi_{\ell} \\ X_{\ell} \end{pmatrix}, \quad \begin{pmatrix} \Phi_{\ell} \\ X_{\ell} \end{pmatrix} = \int_{-\infty}^{\infty} d\bar{p}_y H_{\ell}(\bar{p}_y) \begin{pmatrix} \phi \\ \chi \end{pmatrix}. \quad (61)$$

Substituting the above expansions in Eq. (40) gives:

$$\left( \frac{\partial}{\partial t} + \frac{p_x}{m} \frac{\partial}{\partial x} \right) \begin{pmatrix} \Phi_{\ell} \\ X_{\ell} \end{pmatrix} = -\frac{1}{\tau_*} \begin{pmatrix} \Phi_{\ell} - \Phi_{\ell}^* \\ X_{\ell} - X_{\ell}^* \end{pmatrix}. \quad (62)$$

It can be seen that the moments  $\Phi_{\ell}$  and  $X_{\ell}$  of order  $\ell$  are coupled with those of order  $\ell' \neq \ell$  only through the collision term. However, the equilibrium populations  $\phi_*$  and  $\chi_*$  are determined exclusively by the macroscopic quantities corresponding to the collision invariants,  $n$ ,  $\mathbf{u}$  and  $T$ , as well as  $T_{ij}$  (for the ES model) and  $q_i$  (for the S model). These quantities can be written in terms of the coefficients  $\Phi_{\ell'}$  with  $0 \leq \ell' \leq 3$  and  $X_{\ell'}$  with  $0 \leq \ell' \leq 1$ , as follows:

$$\begin{aligned} \begin{pmatrix} n \\ \rho u_x \\ \rho u_y \end{pmatrix} &= \int_{-\infty}^{\infty} dp_x \begin{pmatrix} \Phi_0 \\ \Phi_0 p_x \\ \Phi_1 p_{0;y} \end{pmatrix}, \\ \begin{pmatrix} T_{xx} \\ T_{xy} \\ T_{yy} \end{pmatrix} &= \int_{-\infty}^{\infty} \frac{dp_x}{m} \begin{pmatrix} \xi_x^2 \Phi_0 \\ \xi_x (\Phi_1 p_{0;y} - m u_y \Phi_0), \\ \Phi_2 p_{0;y}^2 - 2m p_{0;y} u_y \Phi_1 + (p_{0;y}^2 + m^2 u_y^2) \Phi_0 \end{pmatrix}, \\ \begin{pmatrix} \frac{3}{2} n T \\ q_x \end{pmatrix} &= \int_{-\infty}^{\infty} dp_x \begin{pmatrix} 1 \\ \xi_x / m \end{pmatrix} \begin{pmatrix} \frac{\xi_x^2 + p_{0;y}^2 + m^2 u_y^2}{2m} \Phi_0 - p_{0;y} u_y \Phi_1 + \frac{p_{0;y}^2}{2m} \Phi_2 + \frac{1}{2} X_0 \\ \frac{p_{0;y}^3}{2m^2} \Phi_3 - \frac{3p_{0;y}^2 u_y}{2m} \Phi_2 + \frac{p_{0;y}}{2m^2} (\xi_x^2 + 3p_{0;y}^2 + 3m^2 u_y^2) \Phi_1 \\ - \frac{u_y}{2m} (\xi_x^2 + 3p_{0;y}^2 + m^2 u_y^2) \Phi_0 + \frac{p_{0;y}}{2m} X_1 - \frac{u_y}{2} X_0 \end{pmatrix}, \end{aligned} \quad (63)$$

It can be seen that for a given value of  $\ell$ , Eq. (62) involves only terms with  $\ell'$  such that  $0 \leq \ell' \leq \max(\ell, 3)$  for  $\Phi_{\ell}$  and  $0 \leq \ell' \leq \max(\ell, 1)$  for  $X_{\ell}$ . Thus, it can be concluded that the moment system with respect to the  $p_y$  degree of freedom

is closed when the terms up to  $\ell = 3$  and 1 in the series expansions of  $\phi$  and  $\chi$ , respectively, are included. Moreover, the dynamics (and therefore stationary state properties) of the moments in Eq. (63) is recovered exactly when the series for  $\phi$  and  $\chi$  in Eq. (61) are truncated at  $\ell = 3$  and 1, respectively. This truncation is equivalent to considering the quadrature orders  $Q_y^\phi = 4$  and  $Q_y^\chi = 2$ , in the sense that employing higher order quadratures yields results which are exactly equivalent (up to numerical errors due to finite machine precision) to those obtained using  $Q_y^\phi = 4$  and  $Q_y^\chi = 2$ . We discuss below the discretization corresponding to these quadrature orders.

The roots of the Hermite polynomial  $H_4(z) = z^4 - 6z^2 + 3$  of order 4 are known analytically [83]:

$$\begin{aligned}\bar{p}_{y,1}^\phi &= -\sqrt{3 + \sqrt{6}}, & \bar{p}_{y,2}^\phi &= -\sqrt{3 - \sqrt{6}}, \\ \bar{p}_{y,3}^\phi &= \sqrt{3 - \sqrt{6}}, & \bar{p}_{y,4}^\phi &= \sqrt{3 + \sqrt{6}},\end{aligned}\quad (64)$$

where  $\bar{p}_{y,k_y}^\phi \equiv p_{y,k_y}^\phi/p_{0,y}^\phi$  is normalized with respect to an arbitrary scaling factor  $p_{0,y}$ , which we set to 1 in this paper. For the  $\chi$  populations, the discrete momentum components along the  $y$  axis can be found via the roots of  $H_2(z) = z^2 - 1$ :

$$\bar{p}_{y,1}^\chi = -1, \quad \bar{p}_{y,2}^\chi = 1, \quad (65)$$

where  $\bar{p}_{y,s_y}^\chi \equiv p_{y,s_y}^\chi/p_{0,y}^\chi$  and  $p_{0,y}^\chi = 1$ .

The connection between the discrete populations  $\phi_\kappa$  and  $\chi_\sigma$  and their continuous counterparts is given by the 2D extension of Eq. (57):

$$\begin{aligned}\phi_\kappa &= \frac{p_{0,x} w_{k_x}^h(Q_x)}{\omega(\bar{p}_{x,k_x})} \frac{p_{0,y}^\phi w_{k_y}^H(Q_y^\phi)}{\omega(\bar{p}_{y,k_y})} \phi(\bar{p}_{x,k_x}, \bar{p}_{y,k_y}^\phi), \\ \chi_\sigma &= \frac{p_{0,x} w_{s_x}^h(Q_x)}{\omega(\bar{p}_{x,s_x})} \frac{p_{0,y}^\chi w_{s_y}^H(Q_y^\chi)}{\omega(\bar{p}_{y,s_y})} \chi(\bar{p}_{x,s_x}, \bar{p}_{y,s_y}^\chi),\end{aligned}\quad (66)$$

where  $\omega(z)$  is defined in Eq. (58). The quadrature weights for the full-range Gauss-Hermite quadrature can be computed via [43, 49, 50]:

$$w_k^H(Q_y^*) = \frac{Q_y^{*!}}{[H_{Q_y^*+1}(z_k)]^2}, \quad (67)$$

where  $z_k$  ( $1 \leq k \leq Q_y^*$ ) is the  $k$ 'th root of  $H_{Q_y^*}(z)$ . In particular, the weights for  $Q_y^\phi = 4$  and  $Q_y^\chi = 2$  are given by:

$$\begin{aligned} w_{y,1}^H(4) = w_{y,4}^H(4) &= \frac{5 - 2\sqrt{6}}{48}, \\ w_{y,2}^H(4) = w_{y,3}^H(4) &= \frac{5 + 2\sqrt{6}}{48}, \\ w_{y,1}^H(2) = w_{y,2}^H(2) &= \frac{1}{2}. \end{aligned} \quad (68)$$

We now summarize the procedure described above. In the case of the heat transfer problem, the one-dimensional momentum space is discretized following the half-range Gauss-Hermite quadrature prescription using  $Q_x^\phi = Q_x^\chi = Q_x$  quadrature points on each semiaxis for both  $\phi$  and  $\chi$ .

For the shear flow problems, the  $y$  axis of the momentum space is discretized separately for  $\phi$  and  $\chi$ . The total number of quadrature points used to discretize the momentum space for  $\phi$  is  $2Q_x Q_y^\phi = 8Q_x$ , while for  $\chi$ ,  $2Q_x Q_y^\chi = 4Q_x$  quadrature points are required, resulting in a total number of  $12Q_x$  discrete populations.

### 3.3. Projection of the collision term

Part of the lattice Boltzmann paradigm is to replace the local equilibrium distribution by a polynomial expansion, such that the collision invariants  $\psi \in \{1, p_i, \mathbf{p}^2/2m\}$  are exactly preserved. This requires that, after the discretization of the momentum space, the following quadrature sums are exact:

$$\sum_{\boldsymbol{\kappa}} \begin{pmatrix} 1 \\ p_{\boldsymbol{\kappa};i} \end{pmatrix} \phi_{*;\boldsymbol{\kappa}} = \begin{pmatrix} n \\ \rho u_i \end{pmatrix}, \quad \sum_{\boldsymbol{\kappa}} \frac{\xi_{\boldsymbol{\kappa};i} \xi_{\boldsymbol{\kappa};i}}{2m} \phi_{*;\boldsymbol{\kappa}} + \frac{1}{2} \sum_{\boldsymbol{\sigma}} \chi_{*;\boldsymbol{\sigma}} = \frac{3}{2} n T. \quad (69)$$

The above relations can be exactly ensured by first expanding  $\phi_*$  and  $\chi_*$  with respect to the Hermite polynomials (half-range on the  $x$  and full-range on the  $y$  axes, if required), followed by a truncation of the sums at orders  $N_*$ .

In this paper, we follow a hybrid approach. Namely, the equilibrium distributions  $\phi_*$  and  $\chi_*$  are projected onto the set of full-range Hermite polynomials with respect to the axis parallel to the walls (no projection is required in the

case of the heat transfer between stationary plates problem). Then, the expansion coefficients are evaluated directly, following the standard DVM approach. This hybrid approach is motivated as follows.

On the  $x$  axis, the quadrature order  $Q_x$  is considered to be equal for both  $\phi$  and  $\chi$ . Since we are interested in performing simulations in the slip flow and transition regime, we need in general high values of  $Q_x$  (i.e.,  $Q_x \geq 7$  will be required [25]). Let us now assume the equilibrium distributions are expanded with respect to the half-range Hermite polynomials up to order  $N_x = Q_x - 1$ . It is expected that the coefficients of the expansion grow with  $N_x$  as  $\sim N_x! \text{Ma}^{N_x}$ . Since the simulations that we are considering are performed in the non-linear regime, where  $\text{Ma} > 1$ , usually high expansion orders are required (we use  $Q_x = 50$  at  $\delta = 0.1$ ), such that the individual terms in the series expansion can be large. The addition and subtraction of these terms usually leads to a significantly smaller remainder, which can easily be polluted by numerical errors due to finite numerical precision. It is a well-known limitation of the LB algorithm that the polynomial expansion of the equilibrium distribution is not well suited for high-Mach number flows. On the other hand, directly evaluating the equilibrium distributions discussed in Sec. 2.1 when computing the equilibrium moments in Eq. (69) at  $Q_x \geq 7$  is already quite accurate when the half-range Gauss-Hermite quadrature is employed (in this case,  $2Q_x \geq 14$  quadrature points are employed on the  $p_x$  axis). Thus, we find the loss in precision due to the integration via Gauss quadratures of non-polynomial functions via Eq. (69) to be irrelevant.

We further discuss in detail the implementation of the collision term for the  $d = 1$  case encountered in the heat transfer between stationary plates problem (Subsec. 3.3.1). In the  $d = 2$  case, encountered for the Couette flow and heat transfer between moving plates problem, the implementation of the ES and S models is discussed separately in Subsecs. 3.3.2 and 3.3.3, respectively.

### 3.3.1. $d = 1$ case

In the case of the ES model, the equilibrium distribution functions can be found from Eq. (25). When  $d = 1$ , the equilibrium distribution function is

$$\phi_{\text{ES}} = \frac{n}{\sqrt{2\pi mT \mathcal{B}_{xx}}} \exp \left[ -\frac{(p_x - mu_x)^2}{2mT \mathcal{B}_{xx}} \right], \quad (70)$$

while  $\chi_{\text{ES}} = 2T_{\text{red}}\phi_{\text{ES}}$ , where  $T_{\text{red}} = P_{\text{red}}/n$ . In the above,  $\mathcal{B}_{xx}$  and  $P_{\text{red}}$  are given by:

$$\mathcal{B}_{xx} = \frac{1}{\text{Pr}} - \frac{1 - \text{Pr}}{\text{Pr}} \frac{T_{xx}}{P}, \quad P_{\text{red}} = \frac{3}{2}P - \frac{1}{2}T_{xx}. \quad (71)$$

The transition to the discrete system is made via Eq. (66):

$$\phi_{\text{ES};k_x} = \frac{w_{k_x}^{\text{h}}(Q_x)}{\omega(\bar{p}_{x;k_x})} \phi_{\text{ES}}(p_{x;k_x}), \quad \chi_{\text{ES};s_x} = \frac{w_{s_x}^{\text{h}}(Q_x)}{\omega(\bar{p}_{x;s_x})} \chi_{\text{ES}}(p_{x;s_x}), \quad (72)$$

where  $1 \leq k_x, s_x \leq 2Q_x$  and  $\omega(z)$  is defined in Eq. (58).

For the S model, the equilibrium distributions  $\phi_{\text{S}}$  and  $\chi_{\text{S}}$  can be obtained from Eq. (17):

$$\begin{aligned} \phi_{\text{S}} &= \phi_{\text{MB}}(1 + \mathbb{S}_{\phi}), & \chi_{\text{S}} &= 2T\phi_{\text{MB}}(1 + \mathbb{S}_{\chi}), \\ \mathbb{S}_{\phi} &= \frac{1 - \text{Pr}}{5nT^2} \left( \frac{\xi_x^2}{mT} - 3 \right) q_x \xi_x, & \mathbb{S}_{\chi} &= \frac{1 - \text{Pr}}{5nT^2} \left( \frac{\xi_x^2}{mT} - 1 \right) q_x \xi_x, \end{aligned} \quad (73)$$

where  $\xi_x = p_x - mu_x$  and

$$\phi_{\text{MB}} = \frac{n}{\sqrt{2\pi mT}} e^{-\xi_x^2/2mT}. \quad (74)$$

As in Eq. (72), the equilibrium distributions after discretization are computed using:

$$\phi_{\text{S};k_x} = \frac{w_{k_x}^{\text{h}}(Q_x)}{\omega(\bar{p}_{x;k_x})} \phi_{\text{S}}(p_{x;k_x}), \quad \chi_{\text{S};s_x} = \frac{w_{s_x}^{\text{h}}(Q_x)}{\omega(\bar{p}_{x;s_x})} \chi_{\text{S}}(p_{x;s_x}). \quad (75)$$

### 3.3.2. $d = 2$ case: ES model

In the  $d = 2$  case, the exponent  $\mathcal{B}_{ij}^{-1}\xi_i\xi_j$  in Eq. (25) can be written as:

$$\mathcal{B}_{ij}^{-1}\xi_i\xi_j = \mathcal{B}_{yy}^{-1} \left( \xi_y + \frac{\mathcal{B}_{xy}^{-1}}{\mathcal{B}_{yy}^{-1}} \xi_x \right)^2 + \frac{\xi_x^2}{\mathcal{B}_{yy}^{-1}} (\mathcal{B}_{xx}^{-1}\mathcal{B}_{yy}^{-1} - (\mathcal{B}_{xy}^{-1})^2). \quad (76)$$

Noting that the inverse of  $\mathcal{B}_{ij}$  is given by:

$$\mathcal{B}_{ij}^{-1} = \frac{1}{\det \mathcal{B}} \begin{pmatrix} \mathcal{B}_{yy} & -\mathcal{B}_{xy} \\ -\mathcal{B}_{xy} & \mathcal{B}_{xx} \end{pmatrix}, \quad (77)$$

$\phi_{\text{ES}}$  can be factorized as follows:

$$\phi_{\text{ES}} = ng(p_x, u_x, T\mathcal{B}_{xx})g\left(p_y, u_y + \frac{\xi_x \mathcal{B}_{xy}}{m\mathcal{B}_{xx}}, \frac{T \det \mathcal{B}}{\mathcal{B}_{xx}}\right). \quad (78)$$

A similar factorization holds for  $\chi_{\text{ES}} = T_{\text{red}}\phi_{\text{ES}}$ , where  $T_{\text{red}} = P_{\text{red}}/n$  and

$$P_{\text{red}} = 3P - T_{xx} - T_{yy}. \quad (79)$$

We now seek to replace  $\phi_{\text{ES}}$  and  $\chi_{\text{ES}}$  with the expansions  $\phi_{\text{ES}}^{(N_y^\phi)}$  and  $\chi_{\text{ES}}^{(N_y^x)}$  with respect to the Hermite polynomials  $H_\ell(\bar{p}_y)$  containing only terms up to orders  $N_y^\phi$  and  $N_y^x$ , respectively. Defining:

$$\zeta_y = u_y + \frac{\xi_x \mathcal{B}_{xy}}{m\mathcal{B}_{xx}}, \quad T_y = \frac{T}{\mathcal{B}_{xx}} \det \mathcal{B}, \quad (80)$$

Eq. (78) reduces to  $\phi_{\text{ES}} = ng(p_x, u_x, T\mathcal{B}_{xx})g(p_y, \zeta_y, T_y)$ . The trailing function  $g(p_y, \zeta_y, T_y)$  is expanded with respect to  $H_\ell(\bar{p}_y)$  up to order  $N_y^* \in \{N_y^\phi, N_y^x\}$ , as follows:

$$g^{(N_y^*)}(p_y, \zeta_y, T_y) = \frac{\omega(\bar{p}_y)}{p_{0;y}} \sum_{\ell=0}^{N_y^*} \frac{1}{\ell!} H_\ell(\bar{p}_y) \mathcal{G}_\ell. \quad (81)$$

The expansion coefficients  $\mathcal{G}_\ell$  were obtained analytically in Eq. (C.13) in Ref. [43].

Below we reproduce the coefficients for  $0 \leq \ell \leq 3$ :

$$\mathcal{G}_0 = 1, \quad \mathcal{G}_1 = \mathfrak{U}, \quad \mathcal{G}_2 = \mathfrak{U}^2 + \mathfrak{J}, \quad \mathcal{G}_3 = \mathfrak{U}^3 + 3\mathfrak{U}\mathfrak{J}. \quad (82)$$

Identifying  $\mathfrak{U}$  and  $\mathfrak{J}$  from Eq. (C.16) of Ref. [43] with the following expressions,

$$\mathfrak{U} = \frac{m\zeta_y}{p_{0;y}}, \quad \mathfrak{J} = \frac{mT_y}{p_{0;y}^2} - 1, \quad (83)$$

$g^{(2)}(p_y, \zeta_y, T_y)$  necessary for the construction of  $\chi_{\text{ES}}$  can be written as:

$$g^{(2)}(p_y, \zeta_y, T_y) = \frac{\omega(\bar{p}_y)}{p_{0;y}} [H_0(\bar{p}_y) + H_1(\bar{p}_y)\mathfrak{U}]. \quad (84)$$

The function  $g^{(4)}(p_y, \zeta_y, T_y)$  required for  $\phi_{\text{ES}}$ , is given by:

$$g^{(4)}(p_y, \zeta_y, T_y) = \frac{\omega(\bar{p}_y)}{p_{0;y}} \left[ H_0(\bar{p}_y) + H_1(\bar{p}_y)\mathfrak{U} + \frac{1}{2!}H_2(\bar{p}_y) (\mathfrak{U}^2 + \mathfrak{J}) + \frac{1}{3!}H_3(\bar{p}_y) (\mathfrak{U}^3 + 3\mathfrak{U}\mathfrak{J}) \right]. \quad (85)$$

With the above ingredients, after discretization,  $\phi_{\kappa}^{\text{ES}}$  can be evaluated using:

$$\phi_{\kappa}^{\text{ES}} = n \frac{p_{0;x} w_{k_x}^{\text{h}}(Q_x)}{\omega(\bar{p}_{x,k_x})} \frac{p_{0;y} w_{k_y}^{\text{H}}(Q_y)}{\omega(\bar{p}_{y,k_y})} g(p_{x,k_x}, u_x, T\mathcal{B}_{xx}) g^{(4)}(p_{y,k_y}, \zeta_{y;k_x}, T_y), \quad (86)$$

where  $\zeta_{y;k_x} = u_y + \frac{\mathcal{B}_{xy}}{m\mathcal{B}_{xx}} \xi_{x,k_x}$  and  $\xi_{x,k_x} = p_{x,k_x} - mu_x$ . Similarly,  $\chi_{\sigma}^{\text{ES}}$  is:

$$\chi_{\sigma}^{\text{ES}} = P_{\text{red}} \frac{p_{0;x} w_{s_x}^{\text{h}}(Q_x)}{\omega(\bar{p}_{x,s_x})} \frac{p_{0;y} w_{s_y}^{\text{H}}(Q_y)}{\omega(\bar{p}_{y,s_y})} g(p_{x,s_x}, u_x, T\mathcal{B}_{xx}) g^{(2)}(p_{y,s_y}^{\chi}, \zeta_{y;s_x}, T_y). \quad (87)$$

In Eqs. (86) and (87), the function  $g(p_x, u_x, T\mathcal{B}_{xx})$  is evaluated directly. Its expression is reproduced below for convenience:

$$g(p_x, u_x, T\mathcal{B}_{xx}) = \frac{\exp(-\xi_x^2/2mT\mathcal{B}_{xx})}{\sqrt{2\pi mT\mathcal{B}_{xx}}}. \quad (88)$$

### 3.3.3. $d = 2$ case: $S$ model

In the case of the Shakhov model,  $\phi_{\text{S}}$  and  $\chi_{\text{S}}$  can be written as:

$$\phi_{\text{S}} = ng_x g_y (1 + \mathbb{S}_{\phi}), \quad \chi_{\text{S}} = nTg_x g_y (1 + \mathbb{S}_{\chi}), \quad (89)$$

where  $g_x \equiv g(p_x, u_x, T)$  and  $g_y \equiv g(p_y, u_y, T)$  are the one-dimensional Maxwell-Boltzmann distributions introduced in Eq. (2). These functions can be expanded with respect to the full-range Hermite polynomials  $H_{\ell}(\bar{p}_y)$ , as follows:

$$\begin{pmatrix} \phi_{\text{S}} \\ \chi_{\text{S}} \end{pmatrix} = \frac{\omega(\bar{p}_y)}{p_{0;y}} \sum_{\ell=0}^{\infty} \frac{1}{\ell!} H_{\ell}(\bar{p}_y) \begin{pmatrix} \mathcal{G}_{\text{S};\ell}^{\phi} \\ \mathcal{G}_{\text{S};\ell}^{\chi} \end{pmatrix}. \quad (90)$$

The expansion coefficients  $\mathcal{G}_{\text{S};\ell}^{\phi/\chi}$  can be written as:

$$\begin{pmatrix} \mathcal{G}_{\text{S};\ell}^{\phi} \\ \mathcal{G}_{\text{S};\ell}^{\chi} \end{pmatrix} = g_x \begin{pmatrix} n \\ P \end{pmatrix} \left[ \mathcal{G}_{\ell} + \frac{1 - \text{Pr}}{5nT^2} \begin{pmatrix} \mathfrak{G}_{\text{S};\ell}^{\phi} \\ \mathfrak{G}_{\text{S};\ell}^{\chi} \end{pmatrix} \right]. \quad (91)$$

The coefficients  $\mathcal{G}_\ell$  have the same form as in Eq. (82), where the factors  $\mathfrak{U}$  and  $\mathfrak{J}$ , given by Eq. (C.16) in Ref. [43], are reproduced below for convenience:

$$\mathfrak{U} = \frac{mu_y}{p_{0,y}}, \quad \mathfrak{J} = \frac{mT}{p_{0,y}^2} - 1. \quad (92)$$

Denoting:

$$\begin{pmatrix} \mathcal{I}_s^\phi \\ \mathcal{I}_s^\chi \end{pmatrix} = \int_{-\infty}^{\infty} dp_y g(p_y, u_y, T) (q_x \xi_x + q_y \xi_y) \left[ \frac{\xi_x^2 + \xi_y^2}{mT} - \binom{4}{2} \right] \xi_y^s, \quad (93)$$

the coefficients  $\mathfrak{G}_{S;\ell}^{\phi/\chi}$  in Eq. (91) can be obtained as:

$$\begin{aligned} \mathfrak{G}_{S;0}^{\phi/\chi} &= \mathcal{I}_0^{\phi/\chi}, & \mathfrak{G}_{S;1}^{\phi/\chi} &= \frac{1}{p_{0,y}} (\mathcal{I}_1^{\phi/\chi} + mu_y \mathcal{I}_0^{\phi/\chi}), \\ \mathfrak{G}_{S;2}^{\phi/\chi} &= \frac{1}{p_{0,y}^2} [\mathcal{I}_2^{\phi/\chi} + 2mu_y \mathcal{I}_1^{\phi/\chi} + (m^2 u_y^2 - p_{0,y}^2) \mathcal{I}_0^{\phi/\chi}], \\ \mathfrak{G}_{S;3}^{\phi/\chi} &= \frac{1}{p_{0,y}^3} [\mathcal{I}_3^{\phi/\chi} + 3mu_y \mathcal{I}_2^{\phi/\chi} + 3(m^2 u_y^2 - p_{0,y}^2) \mathcal{I}_1^{\phi/\chi} \\ &\quad + mu_y (m^2 u_y^2 - 3p_{0,y}^2) \mathcal{I}_0^{\phi/\chi}]. \end{aligned} \quad (94)$$

Finally, the terms  $\mathcal{I}_s^{\phi/\chi}$  can be obtained by direct integration in Eq. (93):

$$\begin{aligned} \begin{pmatrix} I_0^\phi \\ I_0^\chi \end{pmatrix} &= q_x \xi_x \left[ \frac{\xi_x^2}{mT} - \binom{3}{1} \right], & \begin{pmatrix} I_1^\phi \\ I_1^\chi \end{pmatrix} &= q_y mT \left[ \frac{\xi_x^2}{mT} + \binom{-1}{1} \right], \\ \begin{pmatrix} I_2^\phi \\ I_2^\chi \end{pmatrix} &= q_x \xi_x mT \left[ \frac{\xi_x^2}{mT} + \binom{-1}{1} \right], & \begin{pmatrix} I_3^\phi \\ I_3^\chi \end{pmatrix} &= 3q_y (mT)^2 \left[ \frac{\xi_x^2}{mT} + \binom{1}{3} \right]. \end{aligned} \quad (95)$$

Putting the pieces together, the discrete populations  $\phi_{S;\kappa}$  and  $\chi_{S;\sigma}$  can be computed using:

$$\begin{aligned} \phi_{S;\kappa} &= n \frac{p_{0,x} w_{k_x}^h(Q_x)}{\omega(\bar{p}_{x,k_x})} g(p_{x,k_x}, u_x, T) w_{k_y}^H(4) \sum_{\ell=0}^3 \frac{1}{\ell!} H_\ell(\bar{p}_{y,k_y}^\phi) \left( \mathcal{G}_\ell + \frac{1 - \text{Pr}}{5nT^2} \mathfrak{G}_{S;\ell}^\phi \right), \\ \chi_{S;\sigma} &= nT \frac{p_{0,x} w_{s_x}^h(Q_x)}{\omega(\bar{p}_{x,s_x})} g(p_{x,s_x}, u_x, T) w_{s_y}^H(2) \sum_{\ell=0}^1 \frac{1}{\ell!} H_\ell(\bar{p}_{y,s_y}^\chi) \left( \mathcal{G}_\ell + \frac{1 - \text{Pr}}{5nT^2} \mathfrak{G}_{S;\ell}^\chi \right). \end{aligned} \quad (96)$$

#### 4. Simulation methodology

This section briefly summarizes the methodology employed for obtaining the numerical results discussed in the next sections. Three applications are considered in this paper, namely the heat transfer between stationary plates (Sec. 5), the Couette flow between plates at the same temperature (Sec. 6), and the heat transfer between moving plates (Sec. 7).

In all cases, the simulation results are presented for three values of the rarefaction parameter, namely  $\delta = 10, 1$  and  $0.1$ . For all applications, we take the working gas to be comprised of  $^3\text{He}$  or  $^4\text{He}$  molecules. Additionally, in the case of the heat transfer between moving plates, we also report results for Ne. The reference temperature  $\tilde{T}_{\text{ref}}$ , defined in Eq. (31), varies between 1 K and 3000 K for the  $^3\text{He}$  and  $^4\text{He}$  constituents and between 20 K and 5000 K for the Ne constituents.

Quantitative comparisons are performed by considering a set of dimensionless numbers. In the context of the flows between moving walls (discussed in Sections 6 and 7), the shear stress is used to define the quantity [10]

$$\Pi = -\frac{\tilde{T}_{xy}\tilde{c}_{\text{ref}}}{\tilde{P}_{\text{ref}}\tilde{u}_w\sqrt{2}}. \quad (97)$$

It can be shown that, in the stationary state,  $\Pi$  is constant throughout the channel. In order to access the non-linear regime, we set the wall velocities to  $\tilde{u}_w = \tilde{c}_{\text{ref}}\sqrt{2} = \sqrt{2\tilde{K}_B\tilde{T}_{\text{ref}}/\tilde{m}}$ , such that the Mach number is

$$\text{Ma} = \frac{2\tilde{u}_w}{\tilde{c}_s} \simeq 2.19, \quad (98)$$

where  $\tilde{c}_s = \sqrt{\gamma\tilde{K}_B\tilde{T}_{\text{ref}}/\tilde{m}}$  is the speed of sound and  $\gamma = 5/3$  is the adiabatic index for a monatomic ideal gas. After non-dimensionalization,  $\Pi$  is computed through

$$\Pi = -\frac{1}{2}T_{xy}. \quad (99)$$

In the heat transfer problems, discussed in Sections 5 and 7, the longitudinal heat flux  $\tilde{q}_x$  (perpendicular to the  $x$  axis) is used to introduce

$$Q = -\frac{(\tilde{q}_x + \tilde{T}_{xy}\tilde{u}_y)\tilde{T}_{\text{ref}}}{\tilde{P}_{\text{ref}}\tilde{c}_{\text{ref}}\Delta\tilde{T}\sqrt{2}}, \quad (100)$$

which is again constant throughout the channel. The second term in the numerator vanishes when the walls are stationary (i.e., in Sec. 5). We consider the nonlinear regime, in which the ratio between the temperature difference  $\widetilde{\Delta T} = \widetilde{T}_{\text{right}} - \widetilde{T}_{\text{left}}$  and  $\widetilde{T}_{\text{ref}}$ , defined in Eq. (31), is

$$\frac{\widetilde{\Delta T}}{\widetilde{T}_{\text{ref}}} = 2 \frac{\widetilde{T}_{\text{right}} - \widetilde{T}_{\text{left}}}{\widetilde{T}_{\text{right}} + \widetilde{T}_{\text{left}}} = 1.5. \quad (101)$$

After non-dimensionalization, the wall temperatures are  $T_{\text{left}} = 0.25$  and  $T_{\text{right}} = 1.75$ , while  $Q$  is obtained via:

$$Q = \frac{2\sqrt{2}}{3} \Pi u_y - \frac{\sqrt{2}}{3} q_x. \quad (102)$$

In the context of the Couette flow, we further consider two more quantities. The first is the dimensionless half-channel heat flow rate, defined through

$$Q_y = \frac{2}{\widetilde{L}} \int_0^{\widetilde{L}/2} d\widetilde{x} \frac{\widetilde{q}_y}{\widetilde{P}_{\text{ref}} \widetilde{u}_w}. \quad (103)$$

The second is related to the heat transfer through the domain wall, and is defined through:

$$Q_w = \frac{\widetilde{q}_x(\widetilde{L}/2) \widetilde{c}_{\text{ref}}}{\widetilde{P}_{\text{ref}} \widetilde{u}_w^2 \sqrt{2}} = \frac{\widetilde{u}_y(1/2)}{\widetilde{u}_w} \Pi, \quad (104)$$

where the second equality follows after noting that  $\widetilde{q}_x + \widetilde{T}_{xy} \widetilde{u}_y = 0$  in the stationary state of the Couette flow.

In practice, the quantities  $\Pi$  and  $Q$  exhibit a mild coordinate dependence in the stationary state due to the errors of the numerical scheme. The values reported in the applications sections are obtained by averaging  $\Pi$  and  $Q$  over the simulation domain, as follows:

$$\begin{pmatrix} \Pi \\ Q \end{pmatrix} = \frac{1}{\widetilde{L}} \int_{-\widetilde{L}/2}^{\widetilde{L}/2} d\widetilde{x} \begin{pmatrix} \Pi(\widetilde{x}) \\ Q(\widetilde{x}) \end{pmatrix}. \quad (105)$$

In the case of the Couette flow,  $\Pi(-\widetilde{x}) = \Pi(\widetilde{x})$  is used to reduce the integration domain to  $0 \leq \widetilde{x} \leq \widetilde{L}/2$ .

The LB methodology is discussed in Subsec. 4.1 and the DSMC methodology is summarized in Subsec. 4.2.

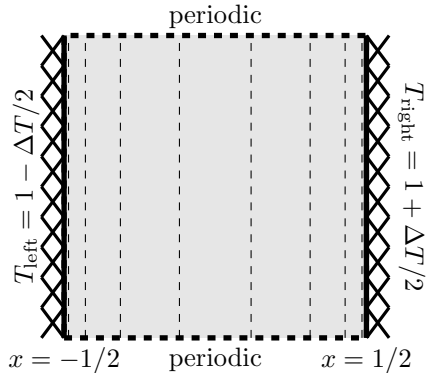


Figure 1: The simulation setup for the heat transfer problem. The vertical dashed lines show a sample grid employing  $S = 4$  points on each half of the channel, stretched according to Eq. (43) with  $A = 0.95$ .

#### 4.1. LB methodology

The LB simulations are performed on a grid comprised of  $S$  cells on the half-channel ( $2S$  cells are used for the heat transfer problems and  $S$  cells are used for the Couette flow simulations). Each cell has the width  $\delta\eta = \text{arctanh}A/S$  with respect to the  $\eta$  coordinate and the stretching parameter is set to  $A = 0.98$ .

At  $\delta = 10$ , the quadrature order on the  $x$  axis is set to  $Q_x = 7$  for the Couette flow and heat transfer between stationary plates problems, while for the heat transfer between moving plates,  $Q_x = 8$  is used. For  $\delta = 1$  and  $0.1$ , the quadrature order is increased to  $Q_x = 11$  and  $50$ , respectively, in order to capture the rarefaction effects.

The simulation is performed until the stationary state is achieved. The time step  $\delta t = 5 \times 10^{-4}$  is always employed and the number of points on the half-channel is set to  $S = 32$  for  $\delta = 10$  and  $1$ , while at  $\delta = 0.1$ ,  $S = 16$  is employed. The number of iterations performed to reach the stationary state is  $60\,000$ ,  $40\,000$  and  $200\,000$  for  $\delta = 10$ ,  $1$  and  $0.1$ , respectively.

In order to assess the accuracy of the simulation results, another set of simulations is performed using  $Q_x = 40$  for  $\delta = 10$  and  $1$ , while for  $\delta = 0.1$ ,  $Q_x = 200$  is employed. The spatial grid is refined by a factor of  $4$ , such that

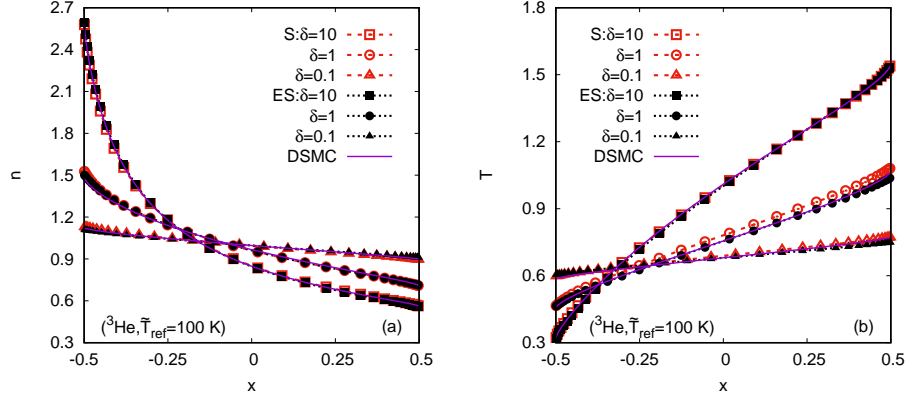


Figure 2: Comparison between the S (red dashed lines and empty symbols) and ES (black dotted lines and filled symbols) results and the DSMC (continuous lines) results in the context of the heat transfer between stationary plates problem for the profiles of (a)  $n$  and (b)  $T$  through the channel ( $-1/2 \leq x \leq 1/2$ ), for  ${}^3\text{He}$  gas constituents. The reference temperature is set to  $\widetilde{T}_{\text{ref}} = 100$  K, while the temperature difference between the two walls is  $\widetilde{\Delta T} = 1.5\widetilde{T}_{\text{ref}}$ .

$S = 128$  is used for  $\delta = 10$  and 1, while for  $\delta = 0.1$ ,  $S = 64$  points are used on the half-channel. The time step in this case is set to  $\delta t = 5 \times 10^{-5}$  for  $\delta = 10$  and 1, and  $\delta t = 4 \times 10^{-5}$  for  $\delta = 0.1$ . We compared the results obtained for  $Q$ ,  $\Pi$ ,  $Q_w$  and  $Q_y$  and found that the relative differences between the results obtained within the two sets of simulations were below 0.1% for all cases under consideration.

In order to compute the integrals over the discretized domain, a fourth order rectangle method is used, summarized below:

$$\begin{aligned} \frac{1}{\widetilde{L}} \int_{-\widetilde{L}/2}^{\widetilde{L}/2} d\widetilde{x} M(\widetilde{x}) &= \frac{1}{A} \int_{-\text{arctanh } A}^{\text{arctanh } A} \frac{d\eta}{\cosh^2 \eta} M(\eta) \\ &= \frac{\text{arctanh } A}{AS} \sum_{s=-S+1}^S \mathbf{f}_s \frac{M_s}{\cosh^2 \eta_s}, \end{aligned} \quad (106)$$

where  $M_s \equiv M(\eta_s)$  and

$$\mathbf{f}_s = \begin{cases} \frac{13}{12}, & s = 4i \text{ or } 4i + 1, \\ \frac{11}{12}, & s = 4i + 2 \text{ or } 4i + 3. \end{cases} \quad (107)$$

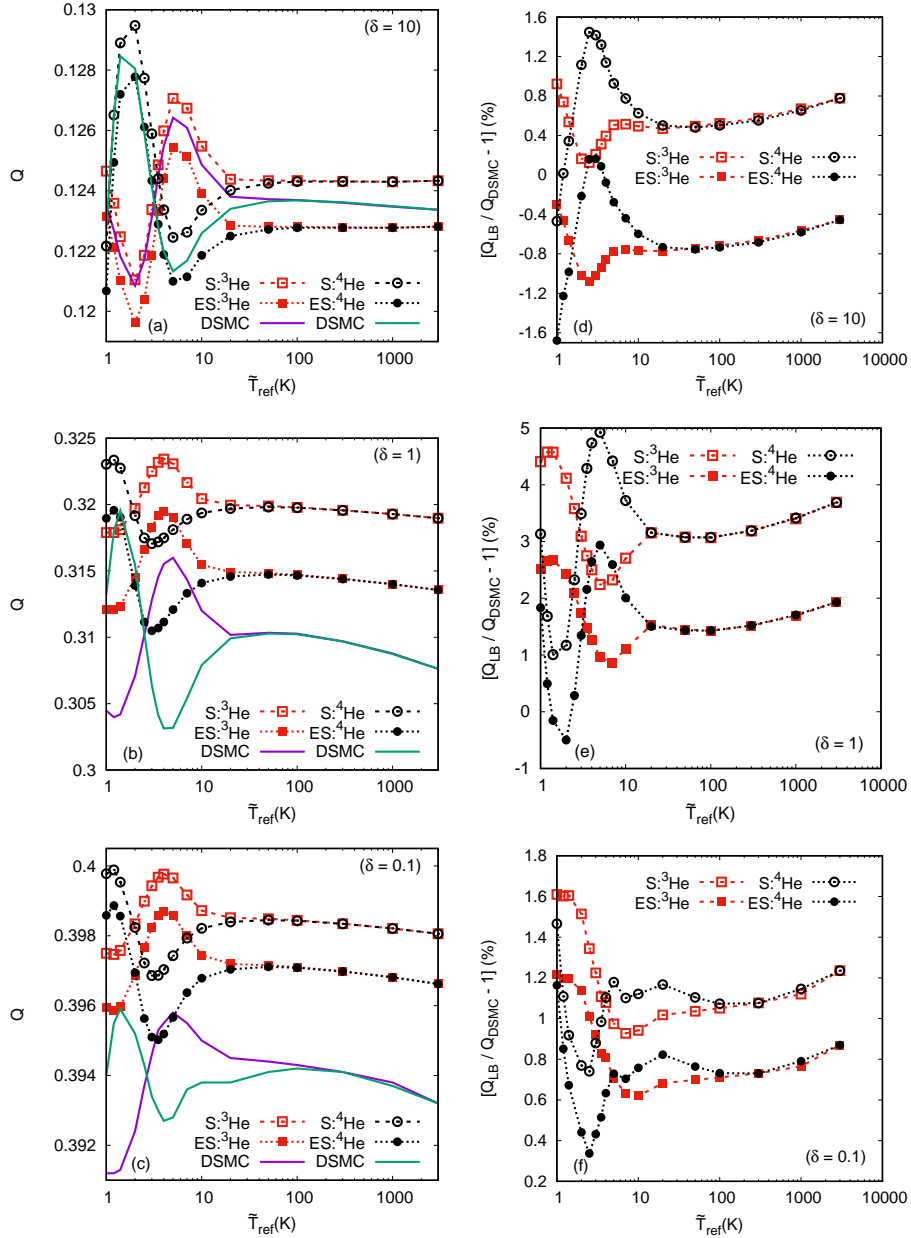


Figure 3: (Left) Dependence of the constant  $Q$ , computed for the heat transfer between stationary plates problem using Eq. (100) with  $\tilde{u}_y = 0$ , on the average wall temperature  $\bar{T}_{\text{ref}}$ . (Right) Relative error  $Q_{\text{LB}}/Q_{\text{DSMC}} - 1$  of the LB results with respect to the DSMC results. Both  $^3\text{He}$  (red dashed lines with squares) and  $^4\text{He}$  (black dotted lines with circles) are considered within the S (empty symbols) and ES (filled symbols) models and the results are represented at  $\delta = 10$  (top), 1 (middle) and 0.1 (bottom).

#### 4.2. DSMC methodology

The DSMC calculations were carried out dividing the space  $-\tilde{L}/2 \leq \tilde{x} \leq \tilde{L}/2$  into 800 cells, considering 200 particles per cell in average, and using the time step  $\delta\tilde{t}$  equal to  $0.002\tilde{L}/\sqrt{2}\tilde{c}_{\text{ref}}$ , where  $\tilde{c}_{\text{ref}} = \sqrt{\tilde{K}_B\tilde{T}_{\text{ref}}/\tilde{m}}$  is defined in Eq. (32). The shear stress  $\Pi$  and heat flux  $Q$ , defined in Eqs. (97) and (100), were calculated by counting the momentum and energy brought and taken away by all particles on both surfaces. To reduce the statistical scattering, the macroscopic quantities were calculated by averaging over  $5 \times 10^5$  samples. These parameters of the numerical scheme provide the total numerical error of  $Q$  and  $\Pi$  less than 0.1%, estimated by carrying out test calculations with the double number of cells, the double number of particles and reducing the time step by a factor of 2. The relative divergence of  $\Pi$  and  $Q$ , calculated on the difference surface using an additional accuracy criterion, does not exceed 0.01%. The details of the numerical scheme and the method used to calculate the look-up tables can be found in Ref. [10].

### 5. Heat transfer

The first application considered in this paper concerns the heat transfer between stationary parallel plates problem. The simulation setup is represented schematically in Fig. 1. In our simulations, the reference temperature,  $\tilde{T}_{\text{ref}} = (\tilde{T}_{\text{left}} + \tilde{T}_{\text{right}})/2$ , is varied between 1 K and 3000 K.

Representative profiles of the density  $n$  and temperature  $T$  are shown for  ${}^3\text{He}$  constituents at  $\tilde{T}_{\text{ref}} = 100$  K in Fig. 2. The DSMC results are shown using solid lines. The LB results obtained with the S model are shown using red dashed lines with empty symbols. The LB results obtained with the ES model are shown using black dotted lines with filled symbols. The LB data corresponding to  $\delta = 10, 1$  and  $0.1$  are shown with squares, circles and triangles, respectively. Very good agreement can be seen between the results obtained using the ES model and the DSMC data. There is a visible discrepancy in the temperature profile obtained with the Shakohv model at  $\delta = 1$ .

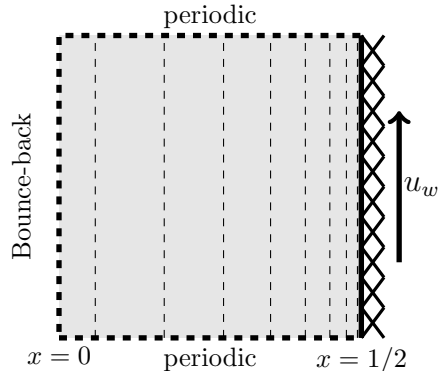


Figure 4: The simulation setup for the Couette flow problem. The vertical dashed lines show a sample grid employing  $S = 8$  points, stretched according to Eq. (43) with  $A = 0.95$ .

A more quantitative analysis is performed at the level of the quantity  $Q$ , introduced in Eq. (100), with  $\tilde{u}_y$  set to 0. Figure 3 compares the LB and DSMC results for  $Q$  with respect to  $T_{\text{ref}}$  for  $1 \text{ K} \leq T_{\text{ref}} \leq 3000 \text{ K}$ , at  $\delta = 10$  (top line), 1 (middle line) and 0.1 (bottom line). On the left column of Fig. 3,  $Q$  is shown in absolute value. On the right column of Fig. 3, the relative error  $Q_{\text{LB}}/Q_{\text{DSMC}} - 1$  is shown. These results were obtained using the S (empty symbols) and the ES (filled symbols) models, for both the  $^3\text{He}$  (red lines with squares) and the  $^4\text{He}$  (black lines with circles) constituents. At  $\delta = 10$ , the S model overestimates the DSMC results. Contrary to the S model, these DSMC results are underestimated by the ES model. The relative errors are roughly the same in absolute values. At smaller values of  $\delta$ , the ES model provides results which are more accurate than those obtained using the S model. The highest relative discrepancy with respect to the DSMC data can be observed at  $\delta = 1$ , when the relative error of the S model reaches almost 5%, while for the ES model, it stays below 3%.

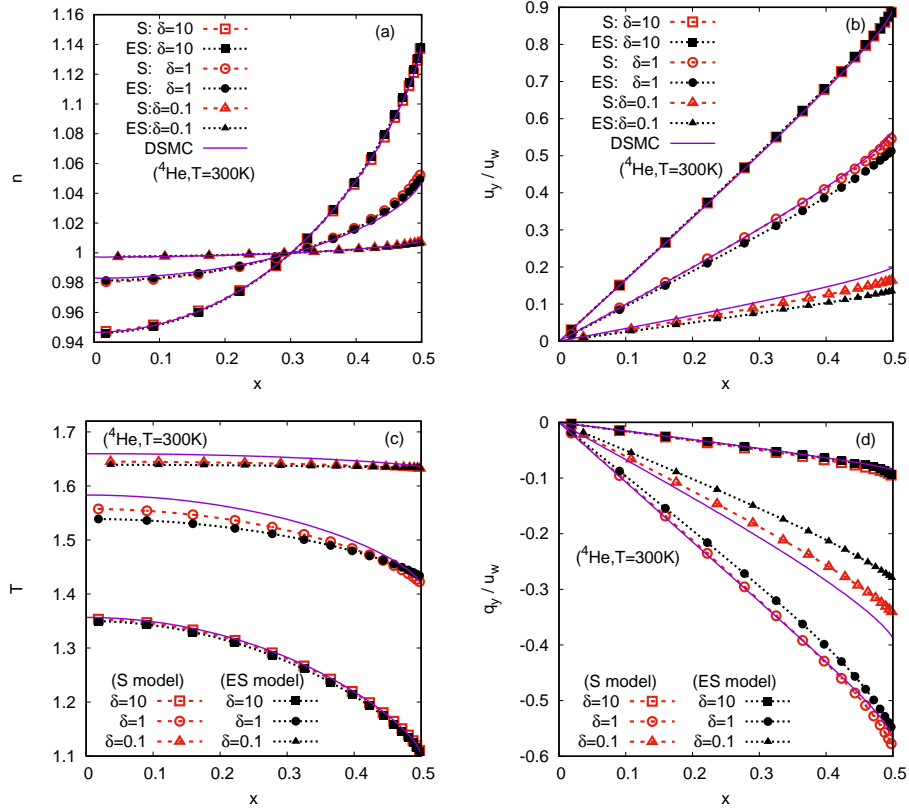


Figure 5: Comparison between the LB results for the S model (dashed red lines and empty symbols) and ES model (dotted black lines and filled symbols) and the DSMC results (continuous lines) for the profiles of (a)  $n$ , (b)  $u_y$ , (c)  $T$  and (d)  $q_y$  through the half-channel ( $0 \leq x \leq 1/2$ ), for  $^4\text{He}$  gas constituents, in the context of the Couette flow. The wall temperature is set to  $\tilde{T}_{\text{ref}} = 300$  K, while the wall velocity is  $u_w = \sqrt{2}$ .

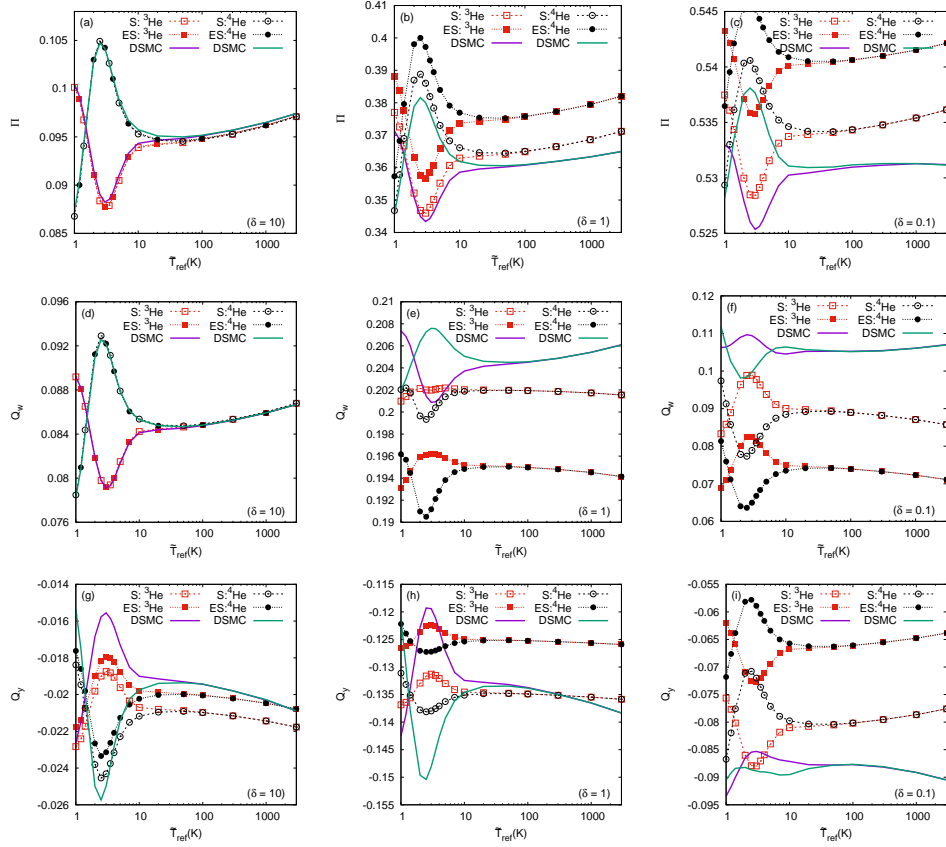


Figure 6: Dependence of  $Q_w$  (top) and  $Q_y$  (bottom), computed in the context of the Couette flow using Eqs. (104) and (103), respectively, on the wall temperature  $\tilde{T}_{\text{ref}}$  for both  $^3\text{He}$  and  $^4\text{He}$ , at  $\delta = 10$  (left), 1 (middle) and 0.1 (right).

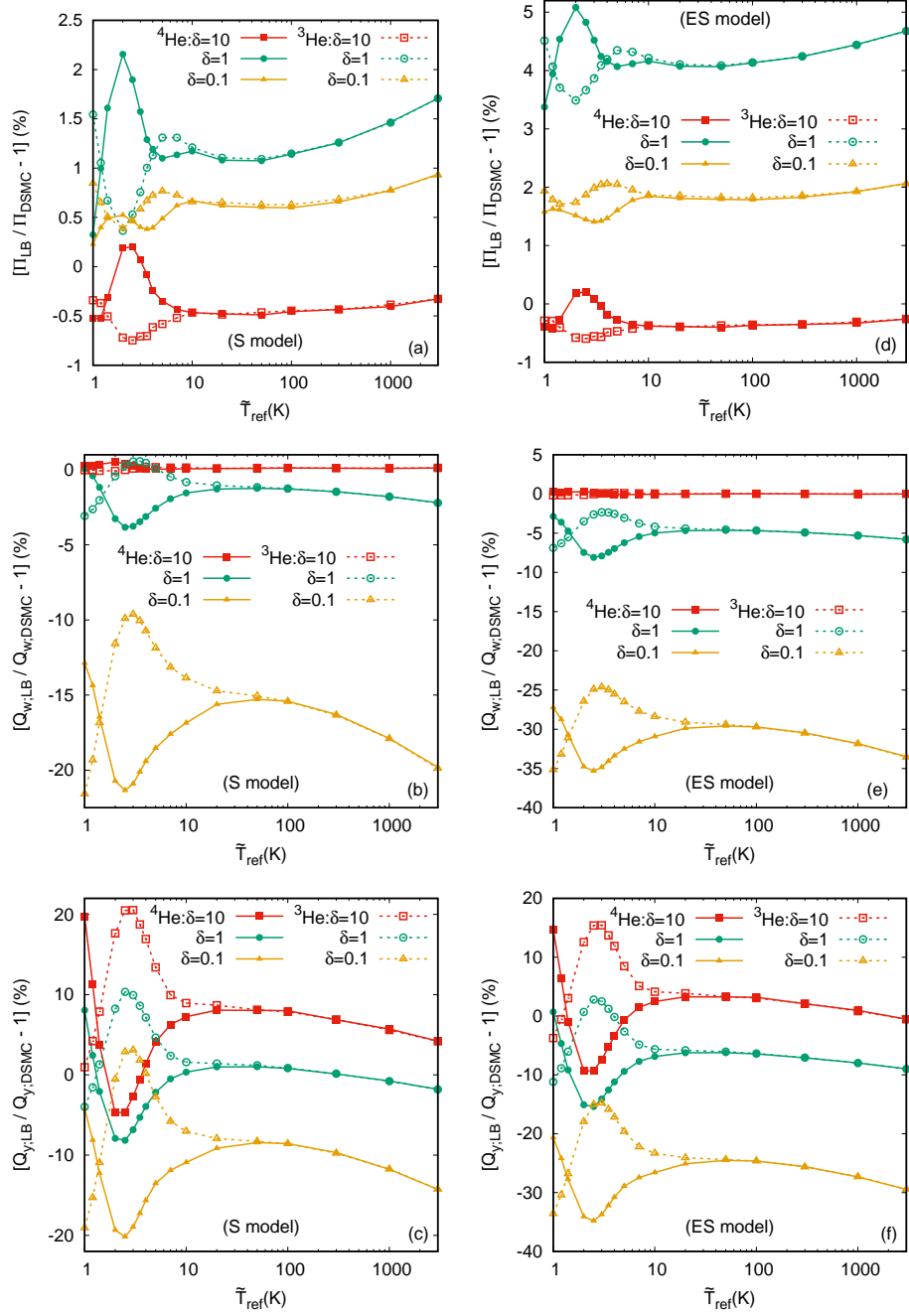


Figure 7: Relative errors  $\Pi_{LB}/\Pi_{DSMC} - 1$  (top),  $Q_{w;LB}/Q_{w;DSMC} - 1$  (middle) and  $Q_{y;LB}/Q_{y;DSMC} - 1$  (bottom) between the DSMC and LB results for the S model (left) and ES model (right), at  $\delta = 10$  (squares), 1 (circles) and 0.1 (triangles) for  $1 \text{ K} \leq T \leq 3000 \text{ K}$ , computed in the context of the Couette flow.<sup>38</sup>

## 6. Couette flow

The second application concerns the Couette flow between parallel plates. Due to the symmetry of the flow, only the right half of the channel ( $0 \leq x \leq 1/2$ ) is considered in the simulation setup, as shown in Fig. 4. The walls are kept at constant temperatures  $\tilde{T}_{\text{left}} = \tilde{T}_{\text{right}} = \tilde{T}_{\text{ref}}$  and  $\tilde{T}_{\text{ref}}$  is varied between 1 K and 3000 K. The wall velocity  $\tilde{u}_w = \sqrt{2\tilde{K}_B\tilde{T}_{\text{ref}}/\tilde{m}}$  takes the value  $u_w = \sqrt{2}$  after non-dimensionalization.

Aside from the transversal component  $q_x$  of the heat flux, which can be related at large  $\delta$  to the temperature variations with respect to the coordinate  $x$  via Fourier's law,  $q_x = -\kappa\partial_x T$ , the Couette flow exhibits a non-vanishing longitudinal heat flux,  $q_y$ , which is a purely microfluidics effect. Figure 5 shows a comparison between the LB results for the S (dashed red lines and empty symbols) and ES (dotted black lines and filled symbols) models and the DSMC results (solid purple lines). The wall temperature is set to  $\tilde{T}_{\text{ref}} = 300$  K and  $^4\text{He}$  gas constituents are considered for  $\delta = 10, 1$  and  $0.1$ . Both the S and ES models are in good agreement with the DSMC data at  $\delta = 10$ . When  $\delta$  decreases, the agreement deteriorates, being slightly worse in the case of the ES model. Remarkably, the density profiles are well recovered with both models at all tested values of  $\delta$ .

We now consider a more quantitative analysis at the level of  $\Pi$ ,  $Q_w$  and  $Q_y$ , computed via Eqs. (97), (104) and (103), respectively. The variation with the plate temperature  $\tilde{T}_{\text{ref}}$  of  $\Pi$  (top),  $Q_w$  (middle) and  $Q_y$  (bottom) for  $^3\text{He}$  and  $^4\text{He}$  is shown in Fig. 6 for  $\delta = 10$  (left column),  $1$  (middle column) and  $0.1$  (right column). Each plot shows curves corresponding to the S model (dashed lines with empty symbols), ES model (dotted lines with filled symbols) and DSMC (solid lines). The data corresponding to  $^3\text{He}$  is shown using red squares, while the data for  $^4\text{He}$  is shown with black circles. It can be seen that in general, the agreement between the results obtained with the model equations and the DSMC results deteriorates as  $\delta$  is decreased. Contrary to the results obtained in the case of the heat transfer problem, the S model gives more accurate results

compared to the ES model, confirming the results reported in Ref. [78]. Figure 7 shows the relative errors computed with respect to the DSMC results, obtained with the S (left column) and ES (right column) models. The results for  $^4\text{He}$  are shown with solid lines and filled symbols, while those for  $^3\text{He}$  are shown with dashed lines and empty symbols. The data corresponding to  $\delta = 10, 1$  and  $0.1$  are shown with red squares, green circles and amber triangles, respectively. In the case of  $\Pi$ , the relative error of the ES model is roughly twice that of the S model.

It is remarkable that the relative errors for both  $Q_w$  and  $Q_y$  reach values around 20% for  $\delta = 0.1$ . This can be explained since the heat fluxes decrease to 0 as  $\delta$  is decreased, while  $\Pi$  attains a finite value as the ballistic regime is approached ( $\lim_{\delta \rightarrow 0} \Pi = \pi^{-1/2}$ ). Thus, the relative errors for  $Q_w$  and  $Q_y$  are computed by dividing the LB values by small numbers. However, in the case of  $Q_y$ , the errors are around 20% even when  $\delta = 10$ , whereas for both  $Q_w$  and  $\Pi$ , the error at  $\delta = 10$  is less than 1%. This disagreement between the model equations and the DSMC data can be attributed to the nature of  $Q_y$ . Since the longitudinal heat flux,  $q_y$ , is not generated by a temperature gradient (through the so-called direct phenomenon), its characteristics must depend on higher order transport coefficients, which are visible only at the Burnett level [84]. Since the model equations are constructed to ensure consistency only at the Navier-Stokes level (corresponding to the first order in the Chapman-Enskog expansion), it is not surprising that such cross phenomena are not accurately recovered.

## 7. Heat transfer under shear

The final example considered in this paper is the heat transfer between parallel plates in motion. The simulation setup is represented in Fig. 8. This example combines the features of the heat transfer between stationary plates discussed in Sec. 5 and those of the Couette flow discussed in Sec. 6. The reference temperature  $\tilde{T}_{\text{ref}} = (\tilde{T}_{\text{left}} + \tilde{T}_{\text{right}})/2$ , is varied between 1 K and 3000 K for  $^3\text{He}$

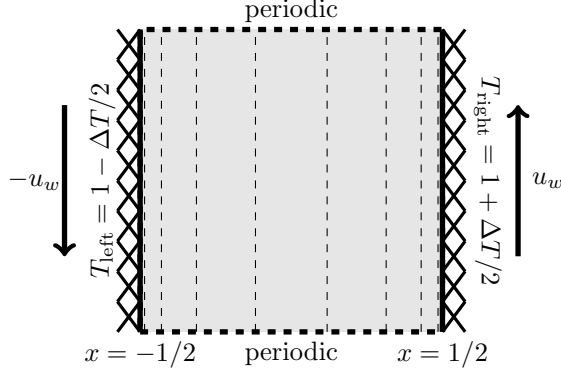


Figure 8: The simulation setup for the heat transfer under shear problem. The vertical dashed lines show a sample grid employing  $S = 4$  points on each half of the channel, stretched according to Eq. (43) with  $A = 0.95$ .

and  ${}^4\text{He}$  constituents, while for Ne, the range for  $\tilde{T}_{\text{ref}}$  is  $20 \text{ K} \leq \tilde{T}_{\text{ref}} \leq 5000 \text{ K}$ . As in Sec. 5, the temperature difference  $\widetilde{\Delta T} = \tilde{T}_{\text{right}} - \tilde{T}_{\text{left}}$  obeys Eq. (101). Furthermore, the plates have velocities  $\tilde{\mathbf{u}}_{\text{left}} = -\tilde{u}_w \mathbf{j}$  and  $\tilde{\mathbf{u}}_{\text{right}} = \tilde{u}_w \mathbf{j}$ , where  $\tilde{u}_w = \sqrt{2\tilde{K}_B \tilde{T}_{\text{ref}} / \tilde{m}}$ , such that the Mach number is given by Eq. (98).

Figure 9 shows the profiles of the density (top row), velocity (middle row) and temperature (bottom row) for the case of Ne constituents at  $T = 300 \text{ K}$ . In general, good agreement can be seen between the results corresponding to the model equations and the DSMC results. A larger discrepancy can be seen between the ES model and the DSMC results, especially in the temperature profile at  $\delta = 1$  and  $0.1$ .

A quantitative analysis can be made at the level of the nondimensional quantities  $\Pi$  and  $Q$ , computed using Eqs. (97) and (100). Figure 10 shows a comparison between the LB results for the S (dashed lines with empty symbols) and the ES (dotted lines with filled symbols) models and the DSMC results (solid lines), obtained for  ${}^3\text{He}$  (squares),  ${}^4\text{He}$  (circles), and Ne (triangles) constituents. Figure 11 shows the relative errors in  $Q$  (dashed lines and empty symbols) and  $\Pi$  (dotted lines and filled symbols) computed for the S model (left column) and ES model (right column) with respect to the DSMC results for  ${}^3\text{He}$  (squares),

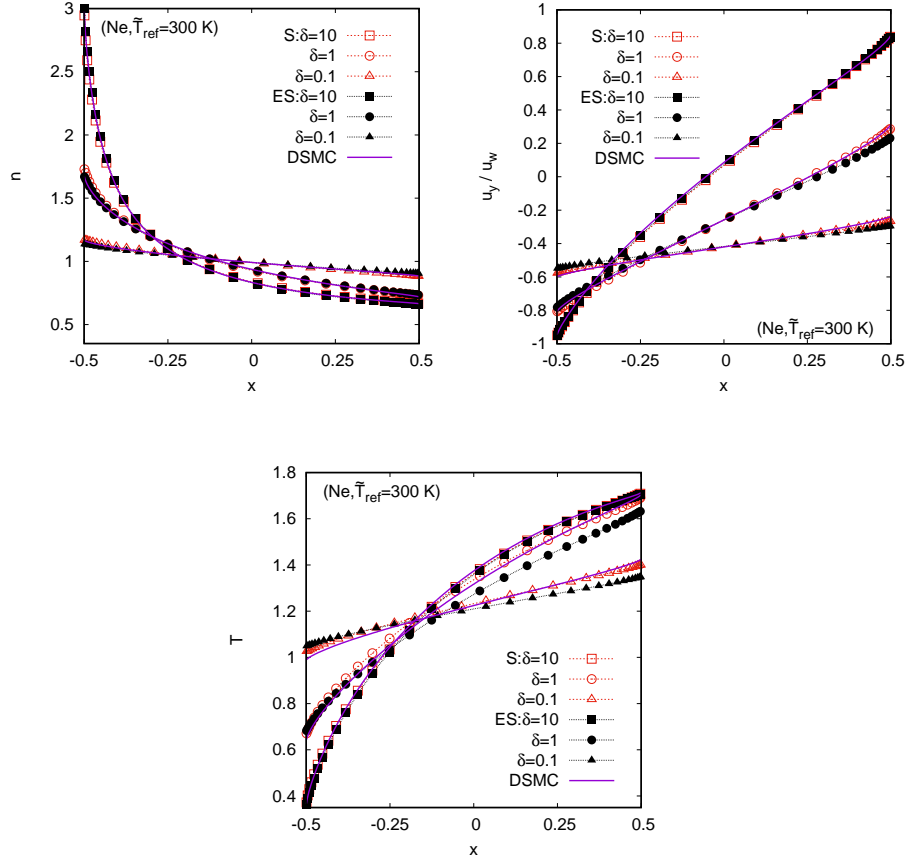


Figure 9: Comparison between the LB results (dotted lines and points) obtained using the S (red empty symbols) and ES (black filled symbols) models and the DSMC (continuous lines) results for the profiles of  $n$  (top),  $u_y$  (middle) and  $T$  (bottom) through the channel ( $-1/2 \leq x \leq 1/2$ ), for Ne gas constituents, in the context of the heat transfer between moving plates problem. The reference temperature is set to  $\tilde{T}_{\text{ref}} = 300$  K, the temperature difference between the two walls is  $\widetilde{\Delta T} = 1.5\tilde{T}_{\text{ref}}$  and the wall velocity is  $\tilde{u}_w = \sqrt{2\tilde{K}_B\tilde{T}_{\text{ref}}/\tilde{m}}$ .

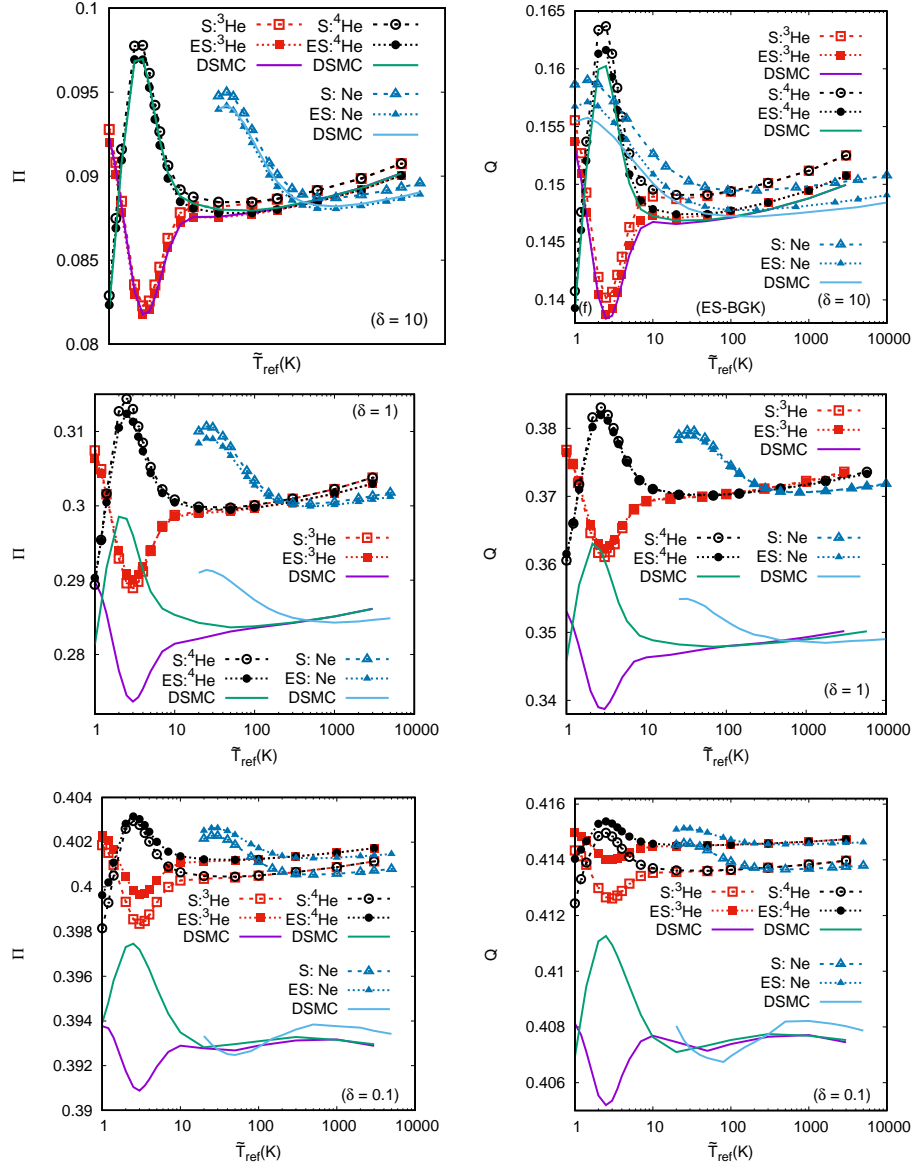


Figure 10: Dependence of  $\Pi$  (left column) and  $Q$  (right column), defined in Eqs. (97) and (100) for the heat transfer between moving plates problem, on the average wall temperature  $\bar{T}_{ref} = (\bar{T}_{left} + \bar{T}_{right})/2$  for  $^3\text{He}$  (red squares),  $^4\text{He}$  (black circles) and Ne (blue triangles), at  $\delta = 10$  (top line), 1 (middle line) and 0.1 (bottom line).

$^4\text{He}$  (circles) and  $\text{Ne}$  (triangles). At  $\delta = 10$  (top line), the results obtained using the ES model seem to be in better agreement with the DSMC results than those obtained using the S model. At  $\delta = 1$  (middle line) and  $0.1$  (bottom line), the two models give results with similar accuracy. As noticed in the case of the heat transfer between stationary plates and in the case of the direct phenomena in the Couette flow, the relative errors are highest at  $\delta = 1$ , where they take values between  $6 - 8\%$  (about  $1\%$  higher for  $Q$  than for  $\Pi$ ).

## 8. Conclusion

In this paper, we presented a systematic comparison between the results obtained using the Boltzmann equation with the Shakhov (S) and Ellipsoidal-BGK (ES) models for the collision term and those obtained using the direct simulation Monte Carlo (DSMC) method for three benchmark channel flows between parallel plates, namely: Couette flow and heat transfer between static and moving walls. The results were obtained numerically in the nonlinear regime [ $\text{Ma} \simeq 2.19$  for the case when the parallel plates are moving and  $2(\tilde{T}_{\text{right}} - \tilde{T}_{\text{left}})/(\tilde{T}_{\text{right}} + \tilde{T}_{\text{left}}) = 1.5$  for the heat transfer problems], by considering  $^3\text{He}$  and  $^4\text{He}$  constituents interacting via *ab initio* potentials. We also consider  $\text{Ne}$  constituents for the heat transfer under shear problem.

In the kinetic theory setup, the connection with the DSMC simulations was made at the level of the transport coefficients (dynamic viscosity  $\tilde{\mu}$  and heat conductivity  $\tilde{\kappa}$ ). For  $^3\text{He}$  and  $^4\text{He}$ , the range of values for the reference temperature  $\tilde{T}_{\text{ref}} = (\tilde{T}_{\text{right}} + \tilde{T}_{\text{left}})/2$  was  $1 \text{ K} \leq \tilde{T}_{\text{ref}} \leq 3000 \text{ K}$ , while for the  $\text{Ne}$  constituents, it was  $20 \text{ K} \leq \tilde{T}_{\text{ref}} \leq 5000 \text{ K}$ . We considered three values for the rarefaction parameter, namely  $\delta = 10$  (slip flow regime),  $\delta = 1$  (transition regime) and  $\delta = 0.1$  (early free molecular flow regime).

We first conducted a qualitative comparison at the level of the profiles of the density, temperature, velocity and heat flux. In all cases considered, the density profile was well recovered with both kinetic models, for all values of the rarefaction parameter. In the context of the heat transfer problem, the results

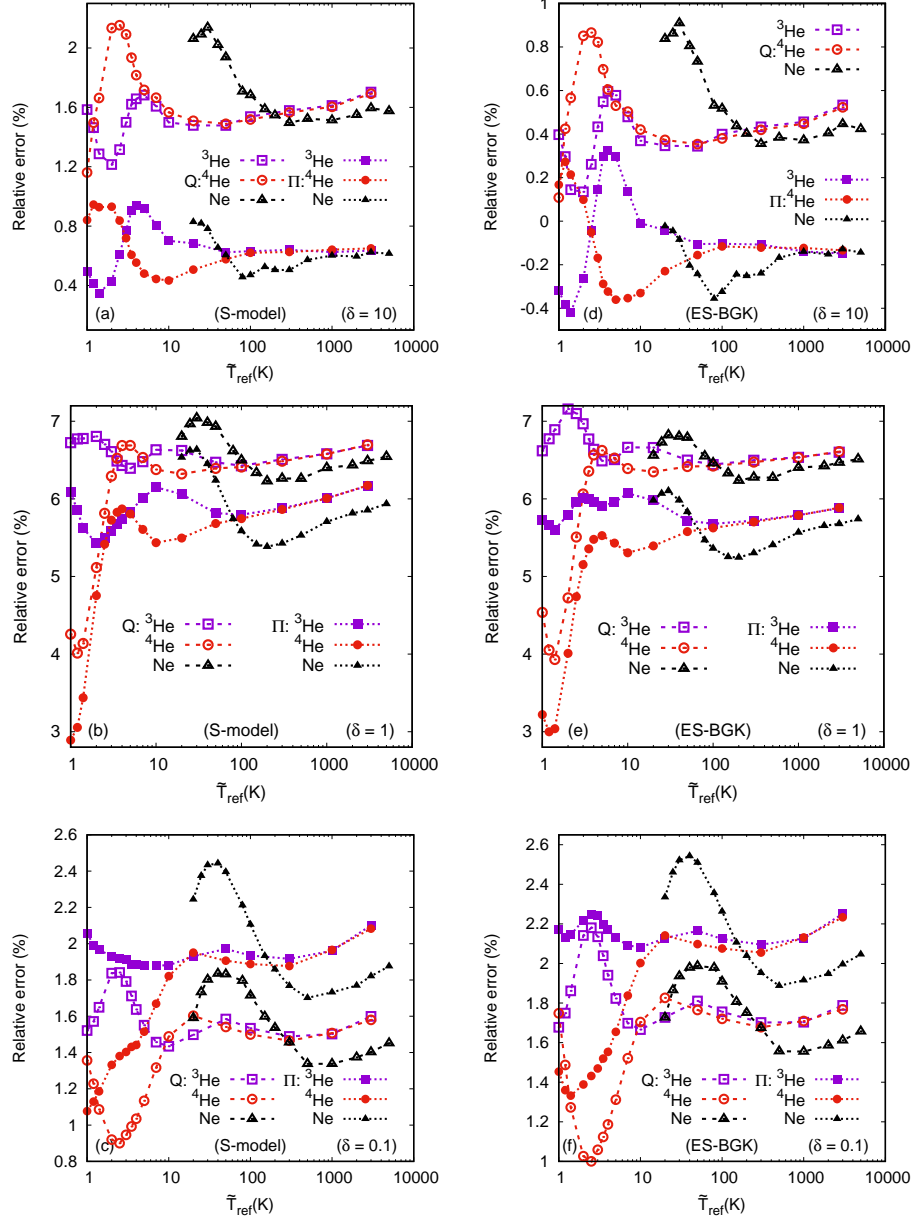


Figure 11: Dependence of the relative errors  $Q_{LB}/Q_{DSMC} - 1$  (dashed lines and empty symbols) and  $\Pi_{LB}/\Pi_{DSMC} - 1$  (dotted lines and filled symbols), expressed in percentages, where the LB results are obtained using the S (left column) and ES (right column) models, for the heat transfer between moving plates problem, on the average wall temperature  $T_{ref} = (T_{left} + T_{right})/2$  for  ${}^3\text{He}$  (squares),  ${}^4\text{He}$  (circles) and Ne (triangles), at  $\delta = 10$  (top line), 1 (middle line) and 0.1 (bottom line).

obtained using the ES model were in better agreement with the DSMC results for the temperature profile. In the Couette and heat transfer with shear problems, the S model seemed to give results which were closer to the DSMC predictions for all quantities (temperature, velocity and heat flux).

We next considered a quantitative comparison of the performance of the kinetic models with respect to the DSMC data by comparing the numerical values for non-dimensional quantities derived from the longitudinal heat flux (in the case of heat transfer between stationary and moving plates, denoted  $Q$ ), shear stress (in the case of Couette flow and heat transfer between moving plates, denoted  $\Pi$ ), as well as the half-channel heat flow rate,  $Q_y$ , and heat transfer rate through the boundary,  $Q_w$  (in the case of the Couette flow). Among these quantities, we can distinguish two categories. The first category (containing  $Q$ ,  $\Pi$  and  $Q_w$ ) refers to quantities related to “direct phenomena,” which are driven by, e.g., shear rate  $\partial_x u_y$  for  $\Pi$  and temperature gradient  $\partial_x T$  for  $Q$ , as predicted by the Navier-Stokes-Fourier theory. The second category (containing  $Q_y$ ) refers to quantities related to “cross phenomena,” visible at the level of the Burnett equations, in which the usual thermodynamic forces driving the non-equilibrium quantity are absent (i.e., non-vanishing  $q_y$  when  $\partial_y T = 0$ ).

For the quantities in the first category (corresponding to direct phenomena), the agreement between the kinetic models and the DSMC results was within a few percent at  $\delta = 10$ , which confirms the validity of these models in the slip flow regime. At  $\delta = 1$ , the errors seem to be bounded within 8% for both models, with the ES model giving better results in the heat transfer between stationary plates problem, while the S model performs better in all other cases. When  $\delta = 0.1$ , the free molecular flow regime is approached. For the quantities that attain a finite value in this regime ( $Q$  in the heat transfer problems and  $\Pi$  in the Couette flow problem), the relative errors drop compared to  $\delta = 1$ , to within 2% – 3%. On the contrary, the relative errors for the heat flux  $Q_w$  measured at the wall in the Couette flow grow to around 20% for the S model and 30% for the ES model. This can be attributed to the fact that  $Q_w$  decreases towards 0 as the free molecular flow regime is approached, such that the relative errors

are computed by dividing the results obtained within the model equations by a small quantity.

When considering the quantity  $Q_y$  from the second category, which is generated through the cross-phenomena, the results of the kinetic models had relative errors of the order of 20% even at  $\delta = 10$ , highlighting that the model equations do not accurately take into account for such phenomena. At  $\delta = 1$ , the relative errors decrease to around 10% for the S model and 15% for the ES model, however they increase again to around 20% and 35% for the S and ES models, respectively. As was the case for  $Q_w$ , the large values encountered at  $\delta = 10$  and  $\delta = 0.1$  may be caused by the fact that  $Q_y$  has vanishing values in the inviscid ( $\delta \rightarrow \infty$ ) and free molecular flow ( $\delta \rightarrow 0$ ) regimes.

In conclusion, our results demonstrate that even in the strongly non-linear regime, the model equations can give reasonably accurate results, with errors of up to 10% for quantities related to direct phenomena throughout the rarefaction spectrum (provided they remain finite in the free molecular flow regime), while the errors for the cross phenomena-related quantities seem to be within 35%. Due to the computational efficiency of the lattice Boltzmann algorithm employed in this paper, solving the kinetic model equations can provide a cheap and reasonably accurate solution for the flow properties in the case of realistic monatomic gases under rarefied conditions.

**Acknowledgments.** VEA gratefully acknowledges the generous support of the Romanian-U.S. Fulbright Commission through The Fulbright Senior Post-doctoral Program for Visiting Scholars 2018-2019, Grant number 678/2018. FS acknowledges the Brazilian Agency CNPq, Brazil, for the support of his research, grant 304831/2018-2. VEA is grateful to Professor P. Dellar (Oxford University, UK) for preliminary discussions regarding the projection of the Shakhov collision term onto orthogonal polynomials. The numerical simulations were performed on the Turing High Performance Computing cluster and the Computing cluster at the Computer Science Department of the Old Dominion University (Norfolk, VA, USA). The computer simulations reported in this paper were done using the Portable Extensible Toolkit for Scientific Computation (PETSc 3.6) developed

at Argonne National Laboratory, Argonne, Illinois [85, 86].

## References

- [1] C. Cercignani. *Rarefied Gas Dynamics: From Basic Concepts to Actual Calculations*. Cambridge University Press, Cambridge, 2000.
- [2] Y. Sone. *Molecular Gas Dynamics: Theory, Techniques and Applications*. Birkhäuser, Boston, 2007.
- [3] S. Takata and H. Funagane. Singular behaviour of a rarefied gas on a planar boundary. *J. Fluid Mech.*, 717:30–47, 2013.
- [4] M. Gad-el-Haq. *MEMS Handbook*. CRC Press, Boca Raton, 2006.
- [5] G. A. Bird. *Molecular Gas Dynamics and the Direct Simulation of Gas Flows*. Oxford University Press, Oxford, 1994.
- [6] F. Sharipov and J. L. Strapasson. Benchmark problems for mixtures of rarefied gases. i. Couette flow. *Phys. Fluids*, 25:027101, 2013.
- [7] F. Sharipov and J. L. Strapasson. *Ab initio* simulation of rarefied gas flow through a thin orifice. *Vacuum*, 109:246–252, 2014.
- [8] F. Sharipov and C. F. Dias. *Ab initio* simulation of planar shock waves. *Computers and Fluids*, 150:115–122, 2017.
- [9] A. N. Volkov and F. Sharipov. Flow of a monatomic rarefied gas over a circular cylinder: Calculations based on the *ab initio* potential method. *Int. J. Heat Mass Transfer.*, 114:47–61, 2017.
- [10] F. Sharipov. Modeling of transport phenomena in gases based on quantum scattering. *Physica A*, 508:797–805, 2018.
- [11] F. Sharipov and C. F. Dias. Temperature dependence of shock wave structure in helium and neon. *Phys. Fluids*, 31:037109, 2019.

- [12] C. Mouhot and L. Pareschi. Fast algorithms for computing the Boltzmann collision operator. *Math. Comput.*, 75:1833–1852, 2006.
- [13] F. Filbet. On deterministic approximation of the Boltzmann equation in a bounded domain. *Multiscale Model. Simul.*, 10:792–817, 2012.
- [14] L. Wu, C. White, T. J. Scanlon, J. M. Reese, and Y. Zhang. Deterministic numerical solutions of the Boltzmann equation using the fast spectral method. *J. Comput. Phys.*, 250:27–52, 2013.
- [15] I. M. Gamba, J. R. Haack, C. D. Hauck, and J. Hu. A fast spectral method for the Boltzmann collision operator with general collision kernels. *SIAM J. Sci. Comput.*, 39:B658–B674, 2017.
- [16] P. L. Bhatnagar, E. P. Gross, and M. Krook. A model for collision processes in gases. i. small amplitude processes in charged and neutral one-component systems. *Phys. Rev.*, 94:511–525, 1954.
- [17] L. H. Holway, Jr. New statistical models for kinetic theory: methods of construction. *Phys. Fluids*, 9:1658–1673, 1966.
- [18] E. M. Shakhov. Generalization of the krook kinetic relaxation equation. *Fluid Dyn.*, 3:95–96, 1968.
- [19] E. M. Shakhov. Approximate kinetic equations in rarefied gas theory. *Fluid Dyn.*, 3:112–115, 1968.
- [20] F. Sharipov. Application of the Cercignani-Lampis scattering kernel to calculations of rarefied gas flows. I. Plane flow between two parallel plates. *Eur. J. Mech. B-Fluid*, 21:113–123, 2002.
- [21] F. Sharipov. Application of the Cercignani-Lampis scattering kernel to calculations of rarefied gas flows. II. Slip and jump coefficients. *Eur. J. Mech. B-Fluid*, 22:133–143, 2003.
- [22] I. A. Graur and A. P. Polikarpov. Comparison of different kinetic models for the heat transfer problem. *Heat Mass Transfer*, 46:237–244, 2009.

- [23] V. E. Ambruş and V. Sofonea. High-order thermal lattice Boltzmann models derived by means of Gauss quadrature in the spherical coordinate system. *Phys. Rev. E*, 86:016708, 2012.
- [24] J. P. Meng, Y. H. Zhang, N. G. Hadjiconstantinou, G. A. Radtke, and X. W. Shan. Lattice ellipsoidal statistical BGK model for thermal non-equilibrium flows. *J. Fluid. Mech.*, 718:347–370, 2013.
- [25] V. E. Ambruş and V. Sofonea. Half-range lattice Boltzmann models for the simulation of Couette flow using the Shakhov collision term. *Phys. Rev. E*, 98:063311, 2018.
- [26] J. E. Broadwell. Study of rarefied shear flow by the discrete velocity method. *J. Fluid Mech.*, 19:401–414, 1964.
- [27] F. Sharipov. *Rarefied gas dynamics: Fundamentals for research and practice*. Wiley-VCH, Weinheim, 2016.
- [28] M. T. Ho and I. Graur. Heat transfer through rarefied gas confined between two concentric spheres. *Int. J. Heat Mass Transfer*, 90:58–71, 2015.
- [29] Z. Guo, K. Xu, and R. Wang. Discrete unified gas kinetic scheme for all Knudsen number flows: Low-speed isothermal case. *Phys. Rev. E*, 88:033305, 9 2013.
- [30] Z. Guo, R. Wang, and K. Xu. Discrete unified gas kinetic scheme for all knudsen number flows. ii. thermal compressible case. *Phys. Rev. E*, 91:033313, 3 2015.
- [31] L. Zhu, P. Wang, and Z. Guo. Performance evaluation of the general characteristics based off-lattice Boltzmann scheme and DUGKS for low speed continuum flows. *J. Comput. Phys.*, 333:227–246, 2017.
- [32] X. He, X. Shan, and G. D. Doolen. Discrete boltzmann equation model for nonideal gases. *Phys. Rev. E*, 57:R13–R16, 1998.

- [33] Z.-H. Li and H.-X. Zhang. Numerical investigation from rarefied flow to continuum by solving the boltzmann model equation. *Int. J. Numer. Meth. Fluids*, 42:361–382, 2003.
- [34] C. Lin, K. H. Luo, L. Fei, and S. Succi. A multi-component discrete Boltzmann model for nonequilibrium reactive flows. *Sci. Rep.*, 7:14580, 2017.
- [35] Y.-D. Zhang, A.-G. Xu, G.-C. Zhang, Z.-H. Chen, and P. Wang. Discrete ellipsoidal statistical BGK model and Burnett equations. *Front. Phys.*, 13:135101, 2018.
- [36] W. P. Yudistiawan, S. Ansumali, and I. V. Karlin. Hydrodynamics beyond Navier-Stokes: The slip flow model. *Phys. Rev. E*, 78:016705, 2008.
- [37] W. P. Yudistiawan, S. K. Kwak, D. V. Patil, and S. Ansumali. Higher-order Galilean-invariant lattice Boltzmann model for microflows: Single-component gas. *Phys. Rev. E*, 82:046701, 2010.
- [38] C. Feuchter and W. Schleifenbaum. High-order lattice Boltzmann models for wall-bounded flows at finite Knudsen numbers. *Phys. Rev. E*, 94:013304, 2016.
- [39] M. Atif, M. Namburi, and S. Ansumali. Higher-order lattice Boltzmann model for thermohydrodynamics. *Phys. Rev. E*, 98:053311, 2018.
- [40] C. K. Aidun and J. R. Clausen. Lattice-Boltzmann method for complex flows. *Annu. Rev. Fluid Mech.*, 42:439–472, 2010.
- [41] J. P. Meng and Y. H. Zhang. Gauss-Hermite quadratures and accuracy of lattice Boltzmann models for nonequilibrium gas flows. *Phys. Rev. E*, 83:036704, 2011.
- [42] Y. Shi, Y. W. Yap, and J. E. Sader. Linearized lattice Boltzmann method for micro- and nanoscale flow and heat transfer. *Phys. Rev. E*, 92:013307, 2015.

- [43] V. E. Ambruş and V. Sofonea. Lattice Boltzmann models based on half-range Gauss-Hermite quadratures. *J. Comput. Phys.*, 316:760–788, 2016.
- [44] S. Succi. *The Lattice Boltzmann Equation for Fluid Dynamics and Beyond*. Clarendon Press, Oxford, 2001.
- [45] P. Fede, V. Sofonea, R. Fournier, S. Blanco, O. Simonin, G. Lepoutère, and V. E. Ambruş. Lattice Boltzmann model for predicting the deposition of inertial particles transported by a turbulent flow. *Int. J. Multiph. Flow*, 76:187–197, 2015.
- [46] T. Krüger, H. Kusumaatmaja, A. Kuzmin, O. Shardt, G. Silva, and E. M. Viggien. *Lattice Boltzmann Method: Principles and Practice*. Springer, 2017.
- [47] S. Succi. *The Lattice Boltzmann Equation: For Complex States of Flowing Matter*. Oxford University Press, 2018.
- [48] X. W. Shan, X. F. Yuan, and H. D. Chen. Kinetic theory representation of hydrodynamics: a way beyond the Navier-Stokes equation. *J. Fluid. Mech.*, 550:413–441, 2006.
- [49] F. B. Hildebrand. *Introduction to Numerical Analysis*. Dover Publications, second edition edition, 1987.
- [50] B. Shizgal. *Spectral Methods in Chemistry and Physics: Applications to Kinetic Theory and Quantum Mechanics (Scientific Computation)*. Springer, 2015.
- [51] E. P. Gross, E. A. Jackson, and S. Ziering. Boundary value problems in kinetic theory of gases. *Ann. Phys.*, 1:141–167, 1957.
- [52] Y. Sone. Kinetic theory analysis of linearized Rayleigh problem. *J. Phys. Soc. Jpn.*, 19:1463–1473, 1964.

- [53] S. Jiang and L.-S. Luo. Analysis and accurate numerical solutions of the integral equation derived from the linearized BGKW equation for the steady Couette flow. *J. Comput. Phys*, 316:416–434, 2016.
- [54] E. P. Gross and S. Ziering. Kinetic theory of linear shear flow. *Phys. Fluids*, 1:215–224, 1958.
- [55] S. Ziering. Shear and heat flow for Maxwellian molecules. *Phys. Fluids*, 3:503–509, 1960.
- [56] P. L. Bhatnagar and M. P. Srivastava. Heat transfer in plane Couette flow of a rarefied gas using Bhatnagar-Gross-Krook model. *Phys. Fluids*, 12:938–940, 1969.
- [57] A. Frezzotti, L. Gibelli, and B. Franzelli. A moment method for low speed microflows. *Continuum Mech. Thermodyn.*, 21:495–509, 2009.
- [58] L. Gibelli. Velocity slip coefficients based on the hard-sphere Boltzmann equation. *Phys. Fluids*, 24:022001, 2012.
- [59] G. P. Ghiroldi and L. Gibelli. A direct method for the Boltzmann equation based on a pseudo-spectral velocity space discretization. *J. Comput. Phys.*, 258:568–584, 2014.
- [60] A. B. Huang and D. P. Giddens. A new table for a modified (half range) GaussHermite quadrature with an evaluation of the integral  $\int_0^\infty e^{-u^2-(z/u)} du$ . *J. Math. Phys.*, 47:213–218, 1968.
- [61] J. S. Ball. Half-range generalized Hermite polynomials and the related Gaussian quadratures. *SIAM J. Numer. Anal.*, 40:2311–2317, 2003.
- [62] Z.-H. Li and H.-X. Zhang. Study on gas kinetic unified algorithm for flows from rarefied transition to continuum. *J. Comput. Phys*, 193:708–738, 2004.
- [63] G. P. Ghiroldi and L. Gibelli. A finite-difference lattice Boltzmann approach for gas microflows. *Commun. Comput. Phys.*, 17:1007–1018, 2015.

- [64] V. E. Ambruş and V. Sofonea. Lattice Boltzmann models based on Gauss quadratures. *Int. J. Mod. Phys. C*, 25:1441011, 2014.
- [65] V. E. Ambruş and V. Sofonea. Implementation of diffuse-reflection boundary conditions using lattice Boltzmann models based on half-space Gauss-Laguerre quadratures. *Phys. Rev. E*, 89:041301(R), 4 2014.
- [66] D. Valougeorgis and S. Naris. Acceleration schemes of the discrete velocity method: Gaseous flows in rectangular microchannels. *SIAM J. Sci. Comput.*, 25:534–552, 2003.
- [67] L. Wu, J. Zhang, H. Liu, Y. Zhang, and J. M. Reese. A fast iterative scheme for the linearized boltzmann equation. *J. Comput. Phys.*, 338:431–451, 2017.
- [68] W. Su, P. Wang, H. Liu, and L. Wu. Accurate and efficient computation of the Boltzmann equation for Couette flow: Influence of intermolecular potentials on Knudsen layer function and viscous slip coefficient. *J. Comput. Phys.*, 378:573–590, 2019.
- [69] Chi-Wang Shu and Stanley Osher. Efficient implementation of essentially non-oscillatory shock-capturing schemes. *J. Comput. Phys.*, 77:439–471, 1988.
- [70] S. Gottlieb and C.-W. Shu. Total variation diminishing runge-kutta schemes. *Math. Comput.*, 67:73–85, 1998.
- [71] J. A. Trangenstein. *Numerical solution of hyperbolic partial differential equations*. Cambridge University Press, New York, 2007.
- [72] V. E. Ambruş and L.-S. Luo. Analysis of knudsen layer phenomena using half-range quadratures. 2019. In preparation.
- [73] R. Mei and W. Shyy. On the finite difference-based lattice Boltzmann method in curvilinear coordinates. *J. Comput. Phys.*, 143:426–448, 1998.

- [74] Z. Guo and T. S. Zhao. Explicit finite-difference lattice Boltzmann method for curvilinear coordinates. *Phys. Rev. E*, 67:066709, 2003.
- [75] S. Busuioc and V. E. Ambruş. Lattice Boltzmann models based on the vielbein formalism for the simulation of flows in curvilinear geometries. *Phys. Rev. E*, 99:033304, 2019.
- [76] C. Cercignani and M. Lampis. Kinetic model for gas-surface interaction. *Transp. Theory Stat. Phys.*, 1:101–114, 1971.
- [77] V. E. Ambruş, F. Sharipov, and V. Sofonea. Lattice Boltzmann approach to rarefied gas flows using half-range Gauss-Hermite quadratures: Comparison to DSMC results based on ab initio potentials. *AIP Conf. Proc.*, 2132:060012, 2019.
- [78] J. Meng, L. Wu, J. M. Reese, and Y. Zhang. Assessment of the ellipsoidal-statistical Bhatnagar-Gross-Krook model for force-driven poiseuille flow. *J. Comput. Phys.*, 251:383–395, 2013.
- [79] W. Cencek, M. Przybytek, J. Komasa, J. B. Mehl, B. Jeziorski, and K. Szalewicz. Effects of adiabatic, relativistic and quantum electrodynamics interactions on the pair potential and thermophysical properties of helium. *J. Chem. Phys.*, 136:224303, 2012.
- [80] F. Sharipov and V. J. Benites. Transport coefficients of helium-neon mixtures at low density computed from *ab initio* potentials. *J. Chem. Phys.*, 147:224302, 2017.
- [81] V. E. Ambruş and V. Sofonea. Quadrature-based lattice Boltzmann models for rarefied gas flow. In F. Toschi and M. Sega, editors, *Flowing Matter*, chapter 9. Springer. in press.
- [82] V. E. Ambruş and V. Sofonea. Application of mixed quadrature lattice Boltzmann models for the simulation of Poiseuille flow at non-negligible values of the Knudsen number. *J. Comput. Sci.*, 17:403–417, 2016.

- [83] V. Sofonea, T. Biciușcă, S. Busuioc, V. E. Ambruș, G. Gonnella, and A. Lamura. Corner-transport-upwind lattice Boltzmann model for bubble cavitation. *Phys. Rev. E*, 97:023309, 2018.
- [84] Jr. W. Marques, G. M. Kremer, and F. M. Sharipov. Couette flow with slip and jump boundary conditions. *Continuum Mech. Thermodyn.*, 12:379–386, 2000.
- [85] Satish Balay, Shrirang Abhyankar, Mark F. Adams, Jed Brown, Peter Brune, Kris Buschelman, Lisandro Dalcin, Victor Eijkhout, William D. Gropp, Dinesh Kaushik, Matthew G. Knepley, Lois Curfman McInnes, Karl Rupp, Barry F. Smith, Stefano Zampini, and Hong Zhang. PETSc users manual. Technical Report ANL-95/11 - Revision 3.6, Argonne National Laboratory, 2015.
- [86] Satish Balay, William D. Gropp, Lois Curfman McInnes, and Barry F. Smith. Efficient management of parallelism in object oriented numerical software libraries. In E. Arge, A. M. Bruaset, and H. P. Langtangen, editors, *Modern Software Tools in Scientific Computing*, pages 163–202. Birkhäuser Press, 1997.